Hydration and bactericidal activity of nanometer- and micrometer-sized particles of rock salt-type Mg1-xCuxO oxides

Batiste Clavier, Téo Baptiste, Zuzana Barbieriková, Tomás Hajdu, Amandine Guiet, Fabien Boucher, Vlasta Brezová, Christine Roques, Gwenaël Corbel

▶ **To cite this version:**

Batiste Clavier, Téo Baptiste, Zuzana Barbieriková, Tomás Hajdu, Amandine Guiet, et al.. Hydration and bactericidal activity of nanometer- and micrometer-sized particles of rock salt-type Mg1-xCuxO oxides. Materials Science and Engineering: C, 2021, 123, pp.111997. 10.1016/j.msec.2021.111997 . hal-03163082

HAL Id: hal-03163082
https://hal.science/hal-03163082

Submitted on 9 Nov 2021

HAL is a multi-disciplinary open access archive for the deposit and dissemination of scientific research documents, whether they are published or not. The documents may come from teaching and research institutions in France or abroad, or from public or private research centers.

L'archive ouverte pluridisciplinaire **HAL**, est destinée au dépôt et à la diffusion de documents scientifiques de niveau recherche, publiés ou non, émanant des établissements d'enseignement et de recherche français ou étrangers, des laboratoires publics ou privés.

Hydration and bactericidal activity of nanometer- and micrometer-sized particles of rock salt-type $Mg_{1-x}Cu_xO$ oxides

Batiste Clavier [1], Téo Baptiste [1], Zuzana Barbieriková [2], Tomáš Hajdu [2], Amandine Guiet [1], Fabien Boucher [3], Vlasta Brezová [2], Christine Roques [4,5] and Gwenaël Corbel [1]*

[1] *Institut des Molécules et Matériaux du Mans (IMMM), UMR-6283 CNRS, Le Mans Université, Avenue Olivier Messiaen, 72085 Le Mans Cedex 9, France*
[2] *Institute of Physical Chemistry and Chemical Physics, Faculty of Chemical and Food Technology, Slovak University of Technology, Radlinského 9, SK-812 37 Bratislava, Slovakia*
[3] *Institut Universitaire de Technologie du Mans, Le Mans Université, Avenue Olivier Messiaen, 72085 Le Mans Cedex 9, France*
[4] *Laboratoire de Génie Chimique, UMR-5503 CNRS, Faculté de Pharmacie, Université Paul Sabatier - Toulouse III, 35, chemin des maraîchers, 31062 Toulouse Cedex 4, France*
[5] *Centre Hospitalier Universitaire (CHU) de Toulouse, Institut Fédératif de Biologie (IFB), Laboratoire de Bactériologie et Hygiène, 330 Avenue de Grande Bretagne, 31059 Toulouse Cedex 9, France*

Abstract

Copper substitution together with nano-structuring are applied with the aim to increase the bactericidal performances of the rocksalt-type MgO oxide. The partial substitution of magnesium ions with Cu^{2+} has been successfully achieved in both micrometer- and nanometer-sized particles of MgO up to 20 mol% in increments of 5 mol%. Microstructural analyses using the Integral Breadth method revealed that the thermal decomposition of the single source precursor $Mg_{1-x}Cu_x(OH)_{2-2y}(CO_3)_y.zH_2O$ at 400°C creates numerous defects in 10–20 nm-sized particles of $Mg_{1-x}Cu_xO$ thus obtained. These defects make the surface of nanoparticles highly reactive towards the sorption of water molecules, to the extent that the cubic cell a parameter in as-prepared $Mg_{1-x}Cu_xO$ expands by +0.24% as soon as the nanoparticles are exposed to ambient air (60% RH). The hydration of $Mg_{1-x}Cu_xO$ particles in liquid water is based on a conventional dissolution-precipitation mechanism. Particles of a few microns in size dissolve all the more slowly the higher the copper content and only $Mg(OH)_2$ starts precipitating after 3 h. In contrast, the dissolution of all 10–20 nm-sized $Mg_{1-x}Cu_xO$ particles is complete over a 3 h period and water suspension only contains 4–12 nm-sized $Mg_{1-x}Cu_x(OH)_2$ particles after 3 h. Thereby, the bactericidal activity reported for water suspension of $Mg_{1-x}Cu_xO$ nanoparticles depends on the speed at which these nanoparticles dissolve and $Mg_{1-x}Cu_x(OH)_2$ nanoparticles precipitate in the first 3 h. Only 10 mol% of cupric ions in MgO nanoparticles are sufficient to kill both *E. coli* and *S. aureus* with a bactericidal kinetics faster and reductions in viability at 3 h (6.5 Log_{10} and 2.7 Log_{10}, respectively) higher than the conventional antibacterial agent CuO (4.7 Log_{10} and 2 Log_{10} under the same conditions). EPR spin trapping study reveals that "hydroxylated" $Mg_{0.9}Cu_{0.1}O$ as well as $Mg_{0.9}Cu_{0.1}(OH)_2$ nanoparticles produce more spin-adducts with highly toxic hydroxyl radicals than their copper-free counterparts. The rapid mass adsorption of $Mg_{0.9}Cu_{0.1}(OH)_2$ nanoparticles onto the cell envelopes following their precipitation together with their ability to produce Reactive Oxygen Species are responsible for the exceptionally high bactericidal activity measured in the course of the hydroxylation of $Mg_{0.9}Cu_{0.1}O$ nanoparticles.

A-Introduction

Bacterial pathogens causing Healthcare-Associated Infections (HAIs) pose ongoing and increasing challenges to hospitals, both in the clinical treatment of patients and in the prevention of their person-to-person transmission. In 2019, a report of the agency "France Public Health" [1] pointed out that four pathogens are responsible for half of the number of HAIs in France: the two Gram-positive bacteria *Staphylococcus aureus* (*S. aureus*, ≈ 13.8%) and *Enterococcus faecalis* (*E. faecalis*, ≈ 6.5%) together with the two Gram-negative bacteria *Escherichia coli*

(*E. coli*, ≈23.6%) and *Pseudomonas aeruginosa* (*P. aeruginosa*, ≈ 6.3%). By designing highly bactericidal compounds having no or very low ecotoxicity, the impact of engineered materials on the environment and the risk of resistance acquisition to antimicrobial agents will be reduced. Nanometer-sized particles of certain oxides such as periclase MgO [2,3] and tenorite CuO [4–6] exhibit bactericidal activity towards these pathogenic bacteria. Due to their long-term geological availabilities, these oxides could substitute with advantage for metallic silver, frequently used as a bactericidal agent. But CuO has ecotoxic effects while MgO has none [7]. Contrary to CuO, a rapid hydration of nanometer-sized MgO particles occurs in aqueous solution [8] leading to a complete conversion into brucite $Mg(OH)_2$ particles over time. The drawback of this hydration is that the reduction in viability of *E. coli* does not exceed 90% (1 Log_{10}) in the best case after 4 h in contact with nanometer-sized $Mg(OH)_2$ particles [9].

Periclase MgO adopts a rock salt-NaCl-type structure (space group F m-3m (No.225)) [10], described as a compact ABCABC stacking of oxygen layers along the [111] direction with magnesium occupying all the regular octahedral interstices. The inter-penetrated Face-Centered-Cubic (FCC) arrays of magnesium and oxygen atoms built up a three dimensional and dense network of edge-sharing $[MgO_6]^{10-}$ octahedra, as shown in Fig. 1a. At reverse, the monoclinic structure of tenorite CuO (space group C2/c (No.15)) can be viewed as a highly distorted NaCl-type structure [11] (Fig. 1b). The distortion originates from the Jahn-Teller effect of cupric ions which induces a huge elongation of the octahedral coordination along its 4-fold axis (four short Cu^{2+}-O equatorial bonds and two long Cu^{2+}-O apical bonds). If such a [4 + 2] distortion is commonly observed in divalent copper compounds, the elongation in tenorite CuO is in magnitude considerable (about 42%). Thereby, cupric ions must be considered in CuO to be 4-fold coordinated to oxide ions (*i.e.* $[CuO_4]^{6-}$) in a square planar geometry (Fig. 1c). Squares at z = 0 share opposite oxygen edges to form infinite $[CuO_3]^{4-}{}_{\infty}$ ribbons running along the [10–1] direction and isolated one from the other in the (*a*,*b*) plane. Theses ribbons at z = 0 are connected by oxygen vertices to similar ribbons at z = 1/2 running along the [101] direction. A regular three-dimensional mesh is thus built up (Fig. 1c). In the literature [12], a solid $Mg_{1-x}Cu_xO$ solution solely exists within the magnesium rich end of the MgO-CuO binary phase diagram. The extent of the solid solution is temperature dependent with a maximum copper content x = 0.20 at 1050 °C. The above structural similarities and differences between MgO and CuO explain why the isovalent substitution of Mg^{2+} ions by cupric ions is only partial in MgO. Ohira et al. [13] showed that micrometer-sized particles of the mixed $Mg_{0.65}Zn_{0.35}O$ oxide exhibit higher bactericidal activities towards the Gram-positive *S. aureus* and the Gram-negative *E. coli* than the parent MgO and ZnO oxides considered separately. Because CuO exhibits both bactericidal activity and stability towards hydration, the partial substitution of magnesium ions by cupric ones could greatly enhance the bactericidal activity of MgO particles while minimizing its sensitivity to hydration.

Recently, we showed that nanometer-sized platelets of several copper-substituted magnesium hydroxides $Mg_{1-x}Cu_x(OH)_{2-2y}(CO_3)_y.zH_2O$ can be simply obtained from metal nitrates by co-precipitation route at room temperature in mixed alkaline medium ($NaOH/Na_2CO_3$) [14]. Temperature-controlled X-ray diffraction study revealed that those nanometer-sized "$Mg_{1-x}Cu_x(OH)_2$" platelets decompose below 400 °C into single mixed periclase-type $Mg_{1-x}Cu_xO$ nanoparticles [14]. It thus gives the opportunity to probe the effects of the nano-structuring and the copper content on the bactericidal activity and sensitivity to hydration of $Mg_{1-x}Cu_xO$ particles. In the present paper, such a study is performed on micrometer- and nanometer-sized particles of $Mg_{1-x}Cu_xO$ ($0 \leq x \leq 0.2$), hereafter referred to "micro-$Mg_{1-x}Cu_xO$" and "nano-$Mg_{1-x}Cu_xO$" series, respectively. For micrometer- and nanometer-sized particles of MgO and $Mg_{0.8}Cu_{0.2}O$, their hydration in water is monitored as a function of immersion time by *ex-situ* X-ray powder diffraction and infrared spectroscopy analyses. For each composition of both series, the evaluation of bactericidal activity is carried out against two bacteria frequently involved in Healthcare-Associated Infections: the Gram-positive *S. aureus* and the Gram-negative *E. coli*. A bactericidal mechanism is finally proposed.

B-Materials and methods

B1. Starting materials

$Mg(NO_3)_2.6H_2O$ (Alfa Aesar, 98%), HNO_3 (VWR Chemicals, 68%), NaOH (Sigma-Aldrich, 98% pellets) and Na_2CO_3 (Acros Organics, 99.8%) were used as received. Commercial CuO (Alfa Aesar, 97%) contains a small amount of cuprous oxide Cu_2O. Prior to use, powder of CuO, spread over the bottom of an alumina boat, was therefore annealed at 600 °C for 12 h in a pure dioxygen gas flow (1 atm) to fully oxidize cuprous ions. Dimethylsulfoxide (DMSO; anhydrous, ≥99.9%), hydrogen peroxide (for analysis, 30%) and 5,5-dimethyl-1-pyrroline *N*-oxide (DMPO) were purchased from Sigma-Aldrich. DMPO was distilled prior to use.

B2. Synthesis of micrometer-sized particles

One gram of micrometer-sized particles of mixed $Mg_{1-x}Cu_xO$ oxides was successfully prepared as a single phase through a modified solid-state reaction route using magnesium and copper nitrates as precursors. The thermal decomposition of magnesium and copper nitrates is used to produce MgO and CuO oxide particles of few hundred nanometers in diameter with a higher reactivity than commercial micrometer-sized oxide particles (Ø ~1–2 μm). The hydration degree of

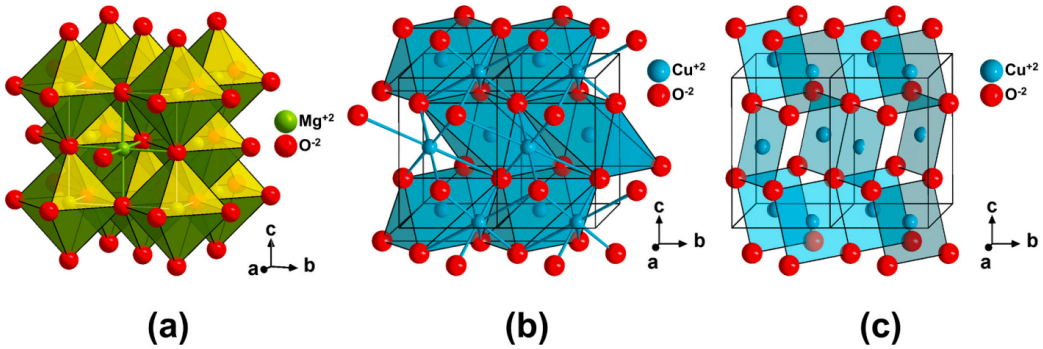

Fig. 1. Perspective view of the crystal structures of MgO (a) and CuO (b and c). Structural description of CuO in terms of octahedral (b) and square planar (c) coordination of cupric ions.

commercial copper nitrate is not always constant, while it is for $Mg(NO_3)_2.6H_2O$. To perfectly control the copper content of the targeted composition, the homogeneous mixture of magnesium and copper nitrates was directly prepared in a Teflon beaker by dissolving CuO and $Mg(NO_3)_2.6H_2O$, weighted in stoichiometric proportion, in 20 mL of concentrated nitric acid (68%). After homogenization for 30 min under stirring, the blue solution was heated up to 140 °C on a hot plate to slowly evaporate the excess of acid and to obtain a blue solid corresponding to intimate mixture of copper and magnesium nitrates. This mixture of nitrates was manually ground in an agate mortar and then transferred into a platinum crucible for subsequent heatings in air. A first annealing for 10 h at 500 °C is carried out to decompose nitrates into oxides (heating rate of 1 °C.min^{-1}). After thoroughly grinding the resulting powder, a single annealing for 10 h at 1050 °C (heating and cooling rates of 5 °C.min^{-1}) was sufficient to achieve a complete solid state reaction between the elementary oxides.

B3. Synthesis of nanometer-sized particles

One gram of nanometer-sized particles of mixed $Mg_{1-x}Cu_xO$ oxides were obtained by decomposing for 12 h at 400 °C in air (heating rate of 3 °C.min^{-1}) the single source precursor $Mg_{1-x}Cu_x(OH)_{2-2y}(CO_3)_y.zH_2O$. These precursors were beforehand prepared at room temperature along a co-precipitation synthetic route extensively described in reference [14]. The optimized decomposition temperature (*i.e.* 400 °C) was determined by ThermoGravimetric (TG) and Mass Spectrometric (MS) evolved gas analyses [14]. Once synthesized, raw nanoparticles were stored in an argon-filled glove box with less than 1 ppm in water to avoid the formation of the by-product hydroxide.

B4. Characterizations and hydration of particles

The different samples were then analyzed by X-ray powder diffraction (XRPD), electron microscopy (SEM, TEM) and nitrogen sorption measurements in order to determine the phase purity, the morphology, the size and the specific surface area of particles. The hydration of both micrometer- and nanometer-sized particles in liquid water and humid air was monitored as a function of time by *ex-situ* XRPD, infrared (IR) spectroscopy and microwave plasma - atomic emission spectroscopy (MP-AES) analyses. Further experimental details about these different analyses are given in Appendix A.

B5. Electron paramagnetic resonance (EPR)

The stock suspensions of MgO, $Mg(OH)_2$, $Mg_{0.9}Cu_{0.1}O$ and $Mg_{0.9}Cu_{0.1}(OH)_2$ nanoparticles (1 mg.mL^{-1}) were prepared in distilled water or DMSO. The spin trapping agent DMPO was dissolved in distilled water or DMSO. The EPR experiments in X-band were performed by means of EMX*plus* spectrometer (Bruker) with a High Sensitivity Probe-head (Bruker) in the small quartz flat cell (WG 808-Q, Wilmad-LabGlass). The suspensions containing nanoparticles at concentration of 1 mg.mL^{-1} were mixed with DMPO and H_2O_2 stock solutions immediately before EPR measurements at 20 °C. In some experiments the prepared suspensions were irradiated directly in the EPR resonator using a UV LED source (λ_{max} = 365 nm, Bluepoint LED, Hönle UV Technology) and the EPR spectra were recorded *in-situ* during exposure. The *g*-values of DMPO spin-adducts were determined with an uncertainty of ±0.0001 using a nuclear magnetic resonance teslameter and integrated frequency counter. The experimental EPR spectra were analyzed by Bruker software WinEPR and the simulated spectra were calculated using the EasySpin toolbox [15]. EPR experiment settings: microwave frequency, ~9.429 GHz; microwave power, 21.4 mW; center field, ~335.8 mT; sweep width, 8 mT; gain, 1.00×10^5–2.52×10^5; modulation amplitude, 0.1 mT; sweep time, 20 s; time constant, 5.12 ms; number of scans, 3–30.

B6. Evaluation of bactericidal activity

The evaluation of the bactericidal activity of the oxide particles was carried out at 20 °C against two strains obtained from the Institute Pasteur Collection (Paris, France): *Staphylococcus aureus* CIP 4.83 and *Escherichia coli* CIP 53126. The strains were stored at −80 °C in Eugon broth (AES, Rennes, France) with 20% (v/v) glycerol (Fluka, Butch, Switzerland). Before each experiment, preserved bacteria were grown at 36 °C under aerobic conditions on trypticase soy agar medium during 24 h (Biomérieux, Craponne, France). The second and third subcultures were used to extemporaneously prepare suspensions with a concentration in bacteria of about 2×10^8 Colony Forming Units per mL (CFU.mL^{-1} calculated from the Optical Density measured at 640 nm). The as-prepared oxide particles were dispersed at 20 °C in sterile distilled water to obtain a suspension with an initial concentration of 1 mg.mL^{-1}. For each strain, 10 mL of each particle suspension are inoculated with 100 µL of bacterial suspension, thus leading to a final concentration in bacteria of $\approx 2 \times 10^6$ CFU.mL^{-1}. A bacterial suspension without particles was used as a positive control. The suspensions were then maintained at 20 °C under constant stirring on a rotary platform working at 250 shakes per min. Permanent agitation of the suspensions prevents the bacteria from adhering to the bottom of the flask and ensures a good aeration of the medium (transfer of dioxygen from air to water). In addition, no sedimentation of (micro- and nano-) particles occurs in our experiments with such agitation. A good distribution of bacteria and particles in the reaction volume is thus achieved. At specified times (15, 30, 60 and 180 min), 1 mL of each suspension and of the corresponding serial ten-fold dilutions were incorporated into trypticase soy agar medium poured in flat-bottomed Petri dishes and plates were incubated at 36 °C for 48 h. The viable cell number was determined by counting the number N of bacterial colonies grown (CFU), multiplied by the dilution factor and expressed as CFU.mL^{-1} of the suspension under test. European Standards for chemical disinfectants and antiseptics (EN 14885) require the expression of the reduction in cell viability in the form of R Log_{10}. Thereby, results are expressed in CFU counts N_t at a contact time t (N_0 at $t = 0$), in percent reduction in cell viability $[(N_0\text{-}N_t) \times 100]/N_0$ as well as in R Log_{10} reduction ($R = Log_{10}(N_0/N_t)$). The experiments were repeated two times for each strain tested. For each contact time tested, control numerations of CFU.mL^{-1} were also performed in sterile distilled water and without particles. The cell viability was preserved for both bacteria in these conditions with CFU counts N_t at t = 15, 30, 60 and 180 min remaining constant regarding the counts N_0 at t = 0 min.

C-Results and discussion

C1. Phase identification of micro- and nanoparticles

Mixed $Mg_{1-x}Cu_xO$ oxides were prepared through two synthetic routes in order to obtain two series of polycrystalline samples with different particles sizes. Whatever the routes, the XRPD patterns of raw powders show single rock-salt MgO-type phase (periclase) in the whole compositional range investigated $0 \leq x \leq 0.2$ (Fig. 2a and b). A shift of all diffraction peaks towards low 2θ scattering angles ($\Delta 2\theta \approx -0.15°$ over the composition range $0 \leq x \leq 0.2$) is noted as the copper content x increases (dashed line in Fig. 2a and b), sign of a homothetic expansion of the cubic unit cell with x. The crystal structures of the different $Mg_{1-x}Cu_xO$ oxides have been refined from their XRPD patterns by the Rietveld method [16] of the Fullprof program [17] using the cubic structure of periclase MgO as a starting structural model [10]. In the crystal structure of MgO, magnesium and oxygen ions lie on 4a (0,0,0) and 4b (½, ½, ½) special positions of the space group F m-3m (No.225), respectively. In the crystal structures of $Mg_{1-x}Cu_xO$, the site occupation factors for Mg and Cu atoms were respectively kept fixed to (1 − x) and x, according to the nominal Cu content x of the analyzed sample. The isotropic thermal factors B_{iso} of all atoms were constrained to the same refined value. All XRPD patterns were satisfactorily modelled by least-

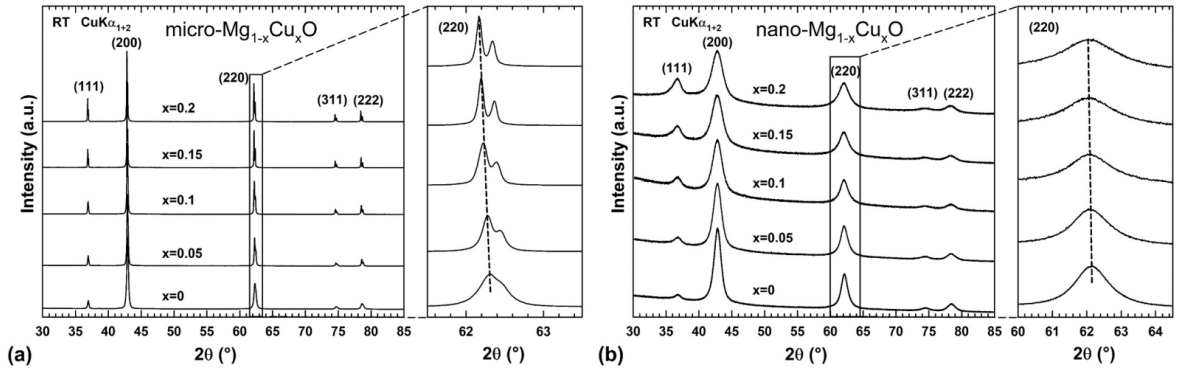

Fig. 2. XRPD patterns collected at ambient air atmosphere (60% RH) and room temperature (RT) on micrometer-sized (a) and nanometer-sized (b) $Mg_{1-x}Cu_xO$ particles for different copper contents x. Insets: effect of the copper content x on the position in 2θ and the profile shape of the (220) diffraction peak.

squares fitting the structural model consisting in three adjustable parameters: the scale factor, the isotropic thermal factors B_{iso} and the cubic cell parameter *a*. The values of those parameters together with conventional reliability factors are reported in Tables S1 and S2 for micro-$Mg_{1-x}Cu_xO$ and nano-$Mg_{1-x}Cu_xO$ samples, respectively (Section 2 in Appendix A). Fig. S1 (Section 2 in Appendix A) shows the final observed, calculated, and difference diffraction patterns of micro-$Mg_{0.8}Cu_{0.2}O$ and nano-$Mg_{0.8}Cu_{0.2}O$, both representative samples of each series. For both series, the evolutions of the cubic cell parameter *a* as a function of the copper content x are displayed in Fig. 3. From the crystal structure of MgO shown in Fig. 1a, the (Mg,Cu)-O bond length is half of the cubic cell parameter *a*. Along the micro-$Mg_{1-x}Cu_xO$ series, the linear expansion of the *a* parameter results from the elongation of (Mg,Cu)-O bonds with increasing the copper content x (usual Vegard's law [18]). This elongation reflects that cupric cation (ionic radius = 0.73 Å (CN = 6) [19]) is slightly larger in size than the Mg^{2+} ion (ionic radius = 0.72 Å (CN = 6) [19]). The existence of this Vegard's law attests the formation of a substitutional solid solution in the whole composition range investigated $0 \leq x \leq 0.2$. Paranthaman et al. [12] have determined the solubility limit of cupric ions in MgO quenched in air from different annealing temperatures ranging from 850 °C to 1050 °C. A maximum in solubility of x = 0.2 is attained at 1050 °C whereas it is more than twice lower at 850 °C with x = 0.09. When samples with a copper content of x = 0.12, 0.15 and 0.17 are quenched from 850 °C, the secondary CuO phase is present in addition to a MgO-type phase. The present study shows that a rate of 5 °C.min^{-1} is fast enough to prevent the exsolution of cupric ions from the rock-salt MgO-type structure when cooling the powders in air from 1050 °C to room temperature.

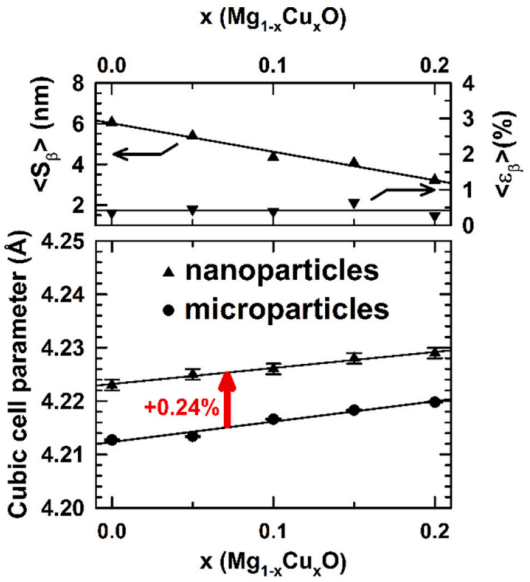

Fig. 3. Variations of the average apparent size $<S_\beta>$ and the average lattice strain $<\varepsilon_\beta>$ of the coherently diffracting domains with the copper content x in nanometer-sized $Mg_{1-x}Cu_xO$ particles. Constant 0.24% expansion of the cubic cell parameter *a* with the nano-structuring of $Mg_{1-x}Cu_xO$ particles for copper content x investigated.

For the nano-$Mg_{1-x}Cu_xO$ series, the dependence of the cubic cell *a* parameter on the copper content x also obeys a Vegard's law, as shown in Fig. 3. However, the nano-structuring of $Mg_{1-x}Cu_xO$ particles induces the same relative lattice expansion (≈ +0.24%) regardless of their copper content x (the Vegard's laws *a* = f(x) for micrometer-sized and nanometer-sized series having the same slope). Razouk and Mikhail [20] have prepared MgO by the decomposition of $Mg(OH)_2$ at different temperatures 350, 500, 800 and 950 °C. They studied the hydration of these oxide particles at 35 °C in relative water vapor pressure P/P_0 varying from zero to saturation [20]. Their results indicate that when MgO particles prepared at 350 °C are exposed for the first time to water vapor, the sorption instantly starts as soon as the relative pressure P/P_0 increases from zero. Because the thermal decomposition of single mixed hydroxide precursors $Mg_{1-x}Cu_x(OH)_{2-2y}(CO_3)_y.zH_2O$ was performed at 400 °C in the present study, one can wonder whether the ≈ +0.24% lattice expansion when reducing the size of $Mg_{1-x}Cu_xO$ particles (Fig. 3) would not originate from a quick surface hydration of nanoparticles at ambient partial water pressure ($P(H_2O)$ ≈ 0.03 atm).

Since bactericidal activity is a surface driven property, any surface hydration of particles necessarily affects their performances, either by degrading or boosting them. The performances as well as the bactericidal mechanism of $Mg_{1-x}Cu_xO$ particles could therefore be different depending on their size and the exposure time to ambient atmosphere. This point is of vital importance for any practical use of bactericidal agent and must be thoroughly investigated. In addition, the bactericidal activity in the present study is evaluated in liquid water at 20 °C. As surface hydration is kinetically faster in liquid water than in ambient air, the stability of the particles must also be monitored when they are immersed in water. Before monitoring the hydration of the particles, their morphology and size were determined by electron microscopy (SEM or TEM). For micrometer- and nanometer-sized particles of MgO and $Mg_{0.8}Cu_{0.2}O$, their stabilities towards water vapor and in liquid water were monitored as a function of exposure/immersion time by *ex-situ* X-ray powder diffraction and infrared spectroscopy analyses. The

two next Sections 3.2 and 3.3 are respectively devoted to these investigations.

C2. Morphology and size of nanoparticles versus microparticles

The SEM micrographs of micrometer-sized particles are displayed in Fig. S2 for the different copper contents x (Section 3 in Appendix A). Irrespective of the copper content, the particles do not have a regular shape or uniform size. Although all powders were annealed at 1050 °C, the particle size is around 1–3 μm for the parent oxide MgO (Fig. S2a), whereas it is ranging from 3 to 10 μm for all copper-containing specimens (Fig. S2b–e). According to literature [21], only subsequent heating of the MgO powder to temperatures between 1300 and 1400 °C would have been able to form particles similar in size to those found in all copper-containing powders. Thereby, the kinetics of grain growth in mixed $Mg_{1-x}Cu_xO$ oxides is faster than in pure MgO. Despite the slight differences in particle size between micro-MgO and micro-$Mg_{1-x}Cu_xO$ (Fig. S2a–e), all the values of the *a* parameter lie on the same Vegard's law (Fig. 3).

The TEM images of the nanometer-sized particles are shown in Fig. 4 for the different copper contents x. These particles have smoothed edges and have no particular shape whether they contain cupric ions (Fig. 4b–e) or not (Fig. 4a). These particles have sizes ranging from ≈10 to 20 nm and form shapeless aggregates. This tendency to particle agglomeration is reminiscent of what was observed when imaging with the transmission electron microscope the nanometer-sized particles of the single source precursors $Mg_{1-x}Cu_x(OH)_{2-2y}(CO_3)_y.zH_2O$ [14] from which the corresponding nano-$Mg_{1-x}Cu_xO$ oxides are derived. For each mixed oxide in the composition range $0 \leq x \leq 0.2$, the selected area electron diffraction (SAED) pattern collected on each aggregate shows four distinct rings, as shown in Fig. 4f for the $x = 0.2$ sample. The presence of rings rather than individual diffraction spots results from the superimposition of the SAED patterns of the numerous nanometer-sized particles forming each aggregate. These four rings are singly indexed to the crystal planes (111), (200), (220) and (311) of a rock-salt MgO-type structure with interreticular d_{hkl} distances in very good agreement with those of the first four Bragg diffraction peaks in the XRPD patterns displayed in Fig. 2b. It thus confirms the high crystallinity of the nanometer-sized $Mg_{1-x}Cu_xO$ particles obtained from the thermal decomposition of the single source precursor $Mg_{1-x}Cu_x(OH)_{2-2y}(CO_3)_y.zH_2O$ at 400 °C. For each nano-$Mg_{1-x}Cu_xO$ oxide, the copper to magnesium atomic ratio, determined by EDX analysis carried out on several single nanoparticles, is in very good agreement with the nominal ratio (Fig. 4g).

In Fig. 2b, all the Bragg peaks have a symmetric Voigt-type profile which makes possible a microstructural analysis from XRPD data using the Integral Breadth method [22–25], as described in details in Appendix A (Section 1.1). In the present analysis, the peak broadening is assumed to originate from both the nanometer size ("size broadening" effect) and the lattice distortion ("microstrain broadening" effect) of coherently diffracting domains. For each nano-$Mg_{1-x}Cu_xO$ oxide, the average apparent size $\langle S_\beta \rangle$ and the average lattice strain $\langle \varepsilon_\beta \rangle$ of these domains were calculated from the integral breadth β of all peaks of their XRPD patterns displayed in Fig. 2b. The variations of $\langle S_\beta \rangle$ and $\langle \varepsilon_\beta \rangle$ as a function of the copper content x in nanometer-sized $Mg_{1-x}Cu_xO$ particles is shown in Fig. 3. In Fig. 3, the average apparent size $\langle S_\beta \rangle$ dropped by half for samples ranging from $x = 0$ to $x = 0.2$ in a linear fashion. In contrast, microstrains are invariant to the copper content x of the mixed oxides with a lattice strain ε_β remaining around 0.4% in average (Fig. 3).

Gordon et al. [26] smashed one $Mg(OH)_2$ crystal of 10–50 μm thick and 1–2 mm large into small pieces (1–5 μm) in order to examine their thermal decomposition under a transmission electron microscope by taking electron micrographs and diffraction patterns at various stages of the process. These authors showed that the dehydroxylation progresses two-dimensionally along the basal (*a,b*) plane of the brucite $Mg(OH)_2$ structure and that shortly after it starts, numerous cracks appear within the entire crystal. In brucite structure, the dehydroxylation of the layers of edge-sharing octahedra stacked along the *c*-axis induces their condensation (oxolation) in order to build up the three dimensional network of edge-sharing octahedra found in the rock-salt-type structure of MgO (Fig. 1a). The (111) and (10−1) lattice planes in MgO are

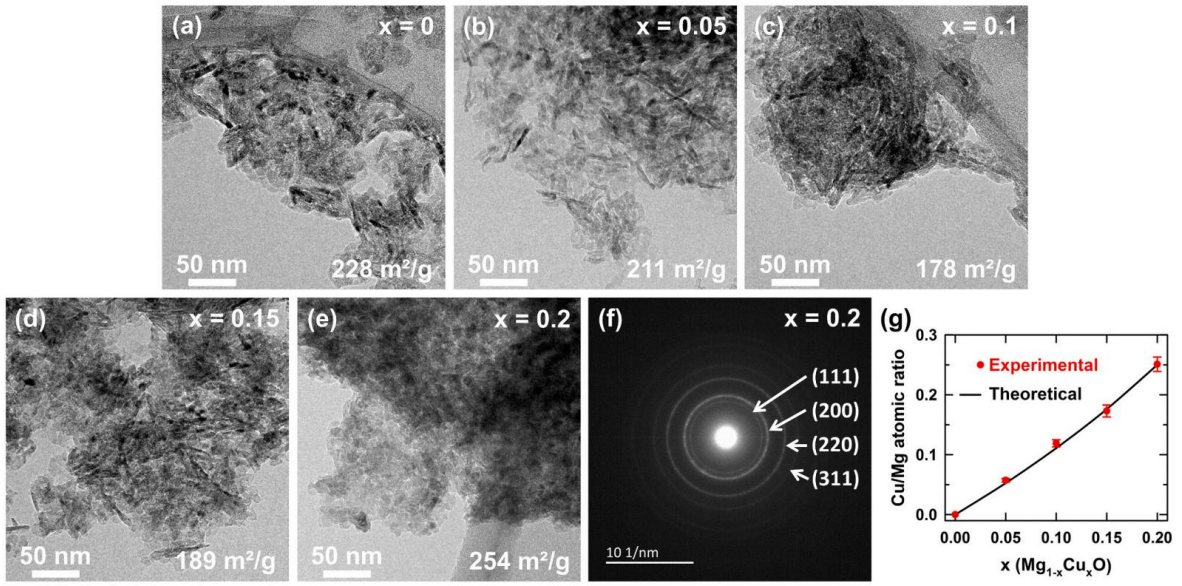

Fig. 4. (a–e) TEM micrographs of nanometer-sized $Mg_{1-x}Cu_xO$ particles for different copper contents x. Specific surface area determined from N_2 adsorption measurements are given. (f) SAED pattern of slightly agglomerated $Mg_{0.8}Cu_{0.2}O$ particles ($x = 0.2$). (g) Evolution of the Cu/Mg atomic ratio determined by EDX analysis as a function of the nominal copper content x in nanometer-sized $Mg_{1-x}Cu_xO$ particles.

directly related to the (0001) and (11−20) lattice planes in $Mg(OH)_2$, respectively [26–28]. During dehydroxylation, lattice strains naturally appear at the reaction interface between just condensed and still hydroxylated layers due to the local reduction of the packing Mg—Mg distance. Dehydroxylation starts at the edges of brucite particle and progresses to the particle core. When it exceeds the tensile strength of brucite particle, the accumulation of lattice strains causes nanoscale cracks which start propagating in the entire particle [26]. After a short period of reaction, the as-produced MgO particles break away from the brucite matrix and stop growing in size. It explains why the MgO particles are smaller in size than $Mg(OH)_2$ ones. In addition, no perfect or complete condensation of layers within the MgO particles inevitably generates nanoscale defects in - or voids between - coherently diffracting domains. The crack and void concentrations depend on the heating rate and temperature as well as the water vapor pressure used for the thermal decomposition of brucite $Mg(OH)_2$ [29].

In a similar way, cracks and voids must appear in the studied nanoparticles when the single source precursor $Mg_{1-x}Cu_x(OH)_{2-2y}(CO_3)_y.zH_2O$ thermally decomposes to form the corresponding $Mg_{1-x}Cu_xO$ oxide. They are at the origin of the high lattice distortions of 0.4% existing in the $Mg_{1-x}Cu_xO$ nanoparticles produced in this way. Because of a constant defect density along the nano-$Mg_{1-x}Cu_xO$ series, the continuous increase in the full width at half maximum (or the integral breadth β) of the Bragg peak (see for instance the (220) peak in Fig. 2b) only originates from the reduction in size of the coherently diffracting domains with increasing x. As expected from the dehydroxylation mechanism detailed above, TEM images show that the $Mg_{1-x}Cu_xO$ particles (≈ 10–20 nm in diameter, Fig. 4) are two times smaller in size than that of $Mg_{1-x}Cu_x(OH)_{2-2y}(CO_3)_y.zH_2O$ ones (≈ 10–50 nm in diameter [14]). Note that, the dimensions of $Mg_{1-x}Cu_xO$ particles measured from TEM micrographs are larger than the average apparent size $<S_\beta>$ of the coherently diffracting domains calculated from XRPD patterns (Fig. 3). Several coherently diffracting domains necessarily coexist within each nanometer-sized particle observed by TEM (Fig. 4a–e). Nitrogen sorption measurements were also carried out to determine the specific surface areas (SAA) of the nanometer-sized particles (Section 1.3 in Appendix A). All nano-$Mg_{1-x}Cu_xO$ powders have high SAA ranging from 180 to 260 $m^2.g^{-1}$ without any particular dependence on the copper content x (Fig. 4a–e).

C3. Hydration of particles in liquid water and humid air: effects of size and copper content

The hydration of particles in liquid water (liquid/solid interaction) and under static humid air atmosphere (gas/solid interaction) is monitored at 20 °C as a function of the immersion/exposure time by *ex-situ* X-ray powder diffraction (XRPD) and infrared (IR) spectroscopy analyses. The experimental conditions are specified in Appendix A (Section 1.4). The experiments in humid air and in liquid water were performed on the micrometer- and nanometer-sized particles of two compositions, MgO and $Mg_{0.8}Cu_{0.2}O$, to determine the effects of the nano-structuring and the copper content of particles on their hydration. The results are addressed below.

C3-a. Hydration in liquid water

The time evolution of XRPD patterns and IR spectra collected on the micrometer- and nanometer-sized particles of MgO and $Mg_{0.8}Cu_{0.2}O$ after their immersion in liquid water are displayed in Fig. 5a and b, respectively. For the micro-MgO sample, three large diffraction peaks ascribed to the hydroxide $Mg(OH)_2$ emerge from the background of XRPD patterns after 180 min of immersion in liquid water (Fig. 5a). Concomitantly, one stretching vibration band ν of hydroxyl group [30] at around 3700 cm^{-1} appears in the IR spectra at the same immersion time (ν_{OH} in Fig. 5b). This frequency of the OH stretching vibration is in very good agreement with the value of 3697 cm^{-1} determined by Martens and Freud on $Mg(OH)_2$ powder [31]. The formation of $Mg(OH)_2$ as the hydration product of MgO is thus confirmed. Although diffraction peaks and ν_{OH} vibration band of $Mg(OH)_2$ grow in intensity with the immersion time, the hydroxylation of micro-MgO particles remains only partial since a large amount of oxide is still detectable by XRPD (Fig. 5a) after 960 min of immersion. The hydroxylation rate α at any immersion time t can be calculated from the decrease in intensity of the (200) Bragg peak of the MgO phase at $2\theta \approx 43°$ (Fig. 5a). This rate is defined by $\alpha = 100 \times (1\text{-}I(200)_t/I(200)_0)$ where $I(200)_t$ and $I(200)_0$ represent the peak intensity at time *t* and 0 min of immersion. As shown in Fig. 5c, the hydroxylation rate α of micro-MgO particles does not exceed ≈ 39% at 960 min.

In the same conditions, no formation of a single $Mg(OH)_2$-type hydroxide is detected on both XRPD patterns and IR spectra collected on the immersed micro-$Mg_{0.8}Cu_{0.2}O$ particles (Fig. 5a and b). Even, if in SEM images (Fig. S2a and e in Appendix A), the micro-$Mg_{0.8}Cu_{0.2}O$ particles are few microns larger in size than the micro-MgO ones, this difference cannot, on its own, explain that no hydroxylation of the micro-$Mg_{0.8}Cu_{0.2}O$ particles occurs after 960 min. This result rather points out that cupric ions significantly slows down the hydroxylation kinetics of the micro-$Mg_{0.8}Cu_{0.2}O$ particles.

As expected, the reduction in particle size below ≈ 20 nm greatly accelerates their hydroxylation kinetics. This acceleration is really significant for nano-$Mg_{0.8}Cu_{0.2}O$ which now behaves in the same way as nano-MgO despite the presence of copper. For both samples, the hydroxylation starts in the first 15 min of immersion in liquid water, as shown in the XRPD patterns and IR spectra (Fig. 5a and b). A single $Mg(OH)_2$-type hydroxide is only observed in the XRPD patterns after 180 min of immersion of both nano-MgO and nano-$Mg_{0.8}Cu_{0.2}O$ particles (Fig. 5a). The hydroxylation is considered complete after 960 min only for nano-MgO particles because the $Mg(OH)_2$ particles precipitated are in equilibrium with a solution saturated in Mg^{2+} at around 6–6.5 $mg.L^{-1}$ for immersion exceeding 180 min (see discussion hereafter). Such steady-state is not reached for hydroxylated $Mg_{0.8}Cu_{0.2}O$ nanoparticles even after 1440 min of immersion (see discussion hereafter). The hydroxylation rate α can be calculated at any immersion time *t* from the intensity of the (011) Bragg peak of the $Mg(OH)_2$ hydroxide located at $2\theta \approx 38°$ in the XRPD patterns. This rate α is defined by $\alpha = 100 \times I(011)_t/I(011)_{960min}$ where $I(011)_t$ and $I(011)_{960min}$ represent the peak intensity at time *t* and 960 min, respectively. As shown in Fig. 5c, the hydroxylation rate α of nano-MgO particles reaches ≈ 91% at 180 min and is greater than 99% after 480 min of immersion of nano-MgO particles. Average apparent sizes $<S_\beta>$ of coherently diffracting domains for those hydroxides were determined from the integral breadth β of all peaks of the XRPD patterns (Fig. 5a). The $Mg(OH)_2$-type hydroxides resulting from the hydroxylation of nano-MgO and nano-$Mg_{0.8}Cu_{0.2}O$ oxides at 180 min have coherently diffracting domains of 12 nm and 4 nm in size, respectively. It is worth noting that the formula of the hydroxide resulting from the hydration of nano-$Mg_{0.8}Cu_{0.2}O$ particles cannot be "$Mg_{0.8}Cu_{0.2}(OH)_2$" because the extent of the solid solution "$Mg_{1-x}Cu_x(OH)_2$" is limited to $x = 0.15$ [14]. As shown in this reference [14], only one small diffraction peak of $Cu(OH)_2$ is present at $2\theta \approx 24°$ in addition to peaks of a major $Mg(OH)_2$-type hydroxide when this solubility limit is exceeded. No trace of $Cu(OH)_2$ is however detected by XRPD (2θ region not shown in Fig. 5a) in the powder recovered by filtration of the water suspension of "hydroxylated nano-$Mg_{0.8}Cu_{0.2}O$ particles" even at this high concentration in particles of 10 $mg.mL^{-1}$. It suggests that the cupric ions in excess must be present in the supernatant (0.059 mol of Cu^{2+} per mole of $Mg_{0.8}Cu_{0.2}O$ converted into 0.94 mol of $Mg_{0.85}Cu_{0.15}(OH)_2$). To verify this assumption, the amounts of magnesium and copper elements released from nano-$Mg_{0.8}Cu_{0.2}O$ particles were measured by atomic emission spectroscopy (AES) after 180 min and 1440 min of immersion in deionized water. Such AES analyses were extended to micrometer-sized particles of MgO and $Mg_{0.8}Cu_{0.2}O$ as well as to nanometer-sized particles of MgO, for comparison purposes. For all samples, a suspension at 1 $mg.mL^{-1}$ in particles was used to perform these AES measurements. This concentration is ten times lower than that

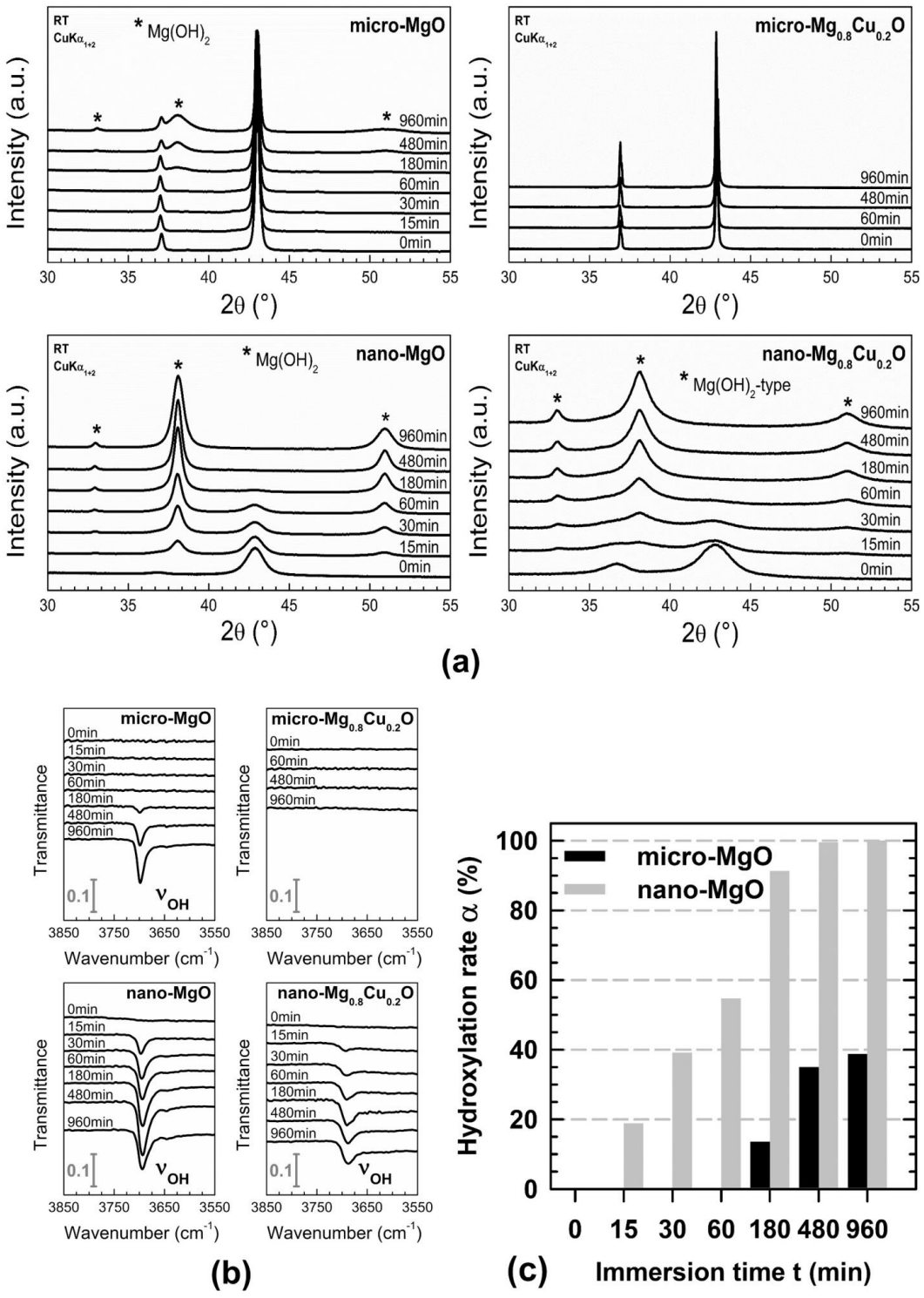

Fig. 5. Evolution of the XRPD patterns (a) and IR transmission spectra (b) collected *ex-situ* and at room temperature (RT) on the micrometer- and nanometer-sized particles of MgO and $Mg_{0.8}Cu_{0.2}O$ after specified time of immersion in liquid water. (c) Time dependence of the hydroxylation rate α for micrometer- and nanometer-sized particles of MgO determined from the XRPD patterns.

chosen for monitoring the hydration of particles by XRPD and IR spectroscopy (10 mg.mL^{-1}). With a suspension at 1 mg.mL^{-1} in particles, the concentration in released cations will still remain in the calibration range used for AES measurements and will thereby avoid multiple dilutions. In addition, such a suspension at 1 mg.mL^{-1} in particles is also used for the evaluation of bactericidal activity (Section 2.6). In parallel, the pH of the supernatant was measured at the same specified time used for monitoring the hydration of particles by XRPD and IR spectroscopy and for evaluating bactericidal performances. The concentrations in divalent cations (Mg^{2+} and Cu^{2+}) and the pH values at the different immersion times are gathered together in Table 1.

In literature [32,33], the hydration of MgO in liquid water is based on a dissolution-precipitation mechanism with three distinct steps detailed below:

(1) the dissociative adsorption of water molecules with the protonation of low-coordinated oxide ions and the hydroxylation of low-coordinated Mg^{2+} ions at surface of MgO particles:

$$MgO_{(s)} + H_2O_{(l)} \rightarrow MgOH^+.OH^-_{(surface)}$$

(2) the surface dissolution with the release of both hydroxide and Mg^{2+} ions into the solution:

$$MgOH^+.OH^-_{(surface)} \rightarrow Mg^{2+}_{(aq)} + OH^-_{(aq)}$$

(3) the precipitation of magnesium hydroxide when the solution is supersaturated in both hydroxide and Mg^{2+} ions: $Mg^{2+}_{(aq)} + OH^-_{(aq)} \rightarrow Mg(OH)_{2(s)}$

In Table 1, the release of hydroxide ions originating from the surface dissolution of MgO particles is responsible for the increase in pH observed in the first 180 min of immersion in liquid water regardless the particle size. The change in pH is larger in magnitude for nanoparticles than for microparticles of MgO because the reduction in size of particles fastens the dissolution kinetics. The solubility of $Mg(OH)_2$ in pure water calculated from its solubility product constant ($K_{sp} = 5.61 \times 10^{-12}$ in [34]) cannot theoretically exceed $\approx 1.12 \times 10^{-4}$ mol.L^{-1} or ≈ 6.53 mg.L^{-1}.

In the supernatant in contact with MgO microparticles for 180 min, the concentration in magnesium overtakes this solubility limit of $Mg(OH)_2$ (Table 1) which reflects a supersaturation of the solution in Mg^{2+}. Concomitantly, $Mg(OH)_2$ starts precipitating after the immersion of MgO microparticles for 180 min, as shown in the XRPD pattern displayed in Fig. 5a. Both results are consistent with the above mentioned dissolution-precipitation mechanism. The concentration in magnesium ions increases in the supernatant between 180 and 1440 min (Table 1). Because the supersaturation of the solution in Mg^{2+} is higher at 1440 min than at 180 min, the slow dissolution of MgO microparticles in water therefore continued in this time period. An immersion time longer than 1440 min is needed to dissolve all MgO microparticles and to reach the equilibrium between the $Mg(OH)_2$ particles precipitated and a solution saturated in Mg^{2+} at around 6–6.5 mg.L^{-1}, as dictated by K_{sp}. One might have expected this dissolution to be complete after 1440 min for a suspension with a mass concentration of particles as low as 1 mg.mL^{-1}. From the above result, it is therefore not surprising that when the mass concentration of particles in the suspension is ten times higher (*i.e.* 10 mg.mL^{-1}), a large fraction of MgO microparticles is still not dissolved and thereby detected by XRPD after 960 min (Fig. 5a). In the supernatant in contact with MgO nanoparticles for 180 min, the concentration in magnesium ions is very close to the solubility limit of $Mg(OH)_2$ in water and remains unchanged after 1440 min (Table 1). An equilibrium between $Mg(OH)_2$ nanoparticles and the solution is this time attained from the first 180 min. This steady-state has only been reached because of the complete dissolution of MgO nanoparticules in liquid water after 180 min, as evidenced by XRPD for the large mass concentration of 10 mg.mL^{-1} in nanoparticles (only the presence of $Mg(OH)_2$ is detected in Fig. 5a).

An increase of two pH units takes place in the first 180 min after the immersion of the micro-$Mg_{0.8}Cu_{0.2}O$ particles in liquid water which is much smaller than the rise in pH from ≈ 5.7 to ≈ 10.5 noted for the micro-MgO sample (Table 1). At 180 min, both the pH value closed to neutrality and the weak concentration in divalent cations released in the supernatant attest that the dissolution of micro-$Mg_{0.8}Cu_{0.2}O$ particles is very limited in magnitude. Even if these microparticles continue to dissolve between 180 and 1440 min, the precipitation of hydroxide cannot occur according to the dissolution-precipitation mechanism since the supersaturation of the solution is far from being reached in this time period (Table 1). This conclusion is supported by the complete absence of a mixed $Mg_{1-x}Cu_x(OH)_2$ hydroxide in the XRPD pattern collected on the micro-$Mg_{0.8}Cu_{0.2}O$ particles immersed for 960 min in liquid water (Fig. 5a). For nano-$Mg_{0.8}Cu_{0.2}O$ particles, the solution remains supersaturated in Mg^{2+} even after 1440 min (Table 1) although only the presence of a $Mg_{1-x}Cu_x(OH)_2$-type hydroxide is detected by XRPD from the first 180 min (Fig. 5a). Such supersaturation in Mg^{2+} is no longer observed for nano-MgO particles beyond 180 min. It suggests that the amount of $Mg_{0.85}Cu_{0.15}(OH)_2$ precipitated is not as large as that of $Mg(OH)_2$ in the first 180 min. When $Mg_{0.8}Cu_{0.2}O$ nanoparticles start dissolving in liquid water, it is expected that the amount of released copper ions is proportional to that of released magnesium ions in compliance with the Cu/Mg ratio of the composition. According to this assumption, the copper concentration in the supernatant calculated from the magnesium concentration should be equal to ≈ 4.9 mg.L^{-1} and ≈ 5.0 mg.L^{-1} after 180 min and 1440 min of immersion, respectively. Surprisingly, the copper concentration in the supernatant is only around 0.3 mg.L^{-1} after 180 min or 1440 min. These low copper concentrations in the supernatant are certainly related to the solubility product constant of $Cu(OH)_2$ in pure water ($K_{sp} = 2.2 \times 10^{-20}$ in [35]) which is much lower than that of $Mg(OH)_2$. As the amount of copper ions in the supernatant is 16 times lower than expected, it implies that either the

Table 1
Time dependencies of the pH and concentrations of magnesium and copper ions in the supernatant after the immersion in water of micrometer- and nanometer-sized particles of both MgO and $Mg_{0.8}Cu_{0.2}O$ oxides (1 mg.mL^{-1}).

Immersion time (min)	MgO				$Mg_{0.8}Cu_{0.2}O$					
	Micro		Nano		Micro			Nano		
	pH	Mg (mg L^{-1})	pH	Mg (mg L^{-1})	pH	Mg (mg L^{-1})	Cu (mg L^{-1})	pH	Mg (mg L^{-1})	Cu (mg L^{-1})
0	5.7	–	5.7	–	5.7	–	–	5.7	–	–
15	8.45	–	9.15	–	6.8	–	–	9.1	–	–
30	8.7	–	9.29	–	6.9	–	–	9.36	–	–
60	9	–	9.33	–	6.96	–	–	9.48	–	–
180	10.53	7.4	10.17	6.1	7.62	1.2	<0.1	9.89	7.5	0.3
480	9.68	–	9.27	–	6.83	–	–	9.22	–	–
1440	9.61	8.3	9.2	6.3	6.96	5.7	<0.1	9.04	7.7	0.3

mixed $Mg_{1-x}Cu_x(OH)_2$ hydroxide formed is richer in copper than the starting oxide $Mg_{0.8}Cu_{0.2}O$ (*i.e.* $x > 0.2$) or that a precipitation of the solvated copper ions occurs with the immersion time and at the basic pH of the supernatant (Table 1). As stated above, the extent of the solid solution "$Mg_{1-x}Cu_x(OH)_2$" is limited to $x = 0.15$ **[14]**. Consequently, only the second hypothesis remains valid. Considering that ≈ 4.9 mg.L^{-1} of cupric ions must have been released by the dissolution of $Mg_{0.8}Cu_{0.2}O$ nanoparticles after 180 min and that only 0.3 mg.L^{-1} remain in the supernatant, we conclude that ≈ 93.9 mol% of the released cupric ions are precipitated mainly as $Mg_{0.85}Cu_{0.15}(OH)_2$ and as $Cu(OH)_2$ presumably for the rest. Whatever the starting mass concentration used 1 or 10 mg.mL^{-1}, the complete absence of $Cu(OH)_2$ from the powder recovered by filtration of the water suspension of "hydroxylated nano-$Mg_{0.8}Cu_{0.2}O$ particles" raises a question (XRPD patterns in Fig. 5a). Cudennec et al. **[36]** found that in pure water, the copper hydroxide remains stable and blue in color for several weeks before first darkening and then decomposing into CuO. These authors also noticed that a progressive dissolution of $Cu(OH)_2$ particles occurs with time in hydroxide ions rich-medium, leading to the formation of the soluble square planar $[Cu(OH)_4]^{2-}$ complex **[37]**. These $[Cu(OH)_4]^{2-}$ anions give rise to copper oxide CuO particles in a few hours through a condensation/dehydration process. Of course, such precipitation of CuO cannot be ruled out in the basic medium generated by the dissolution of nano-$Mg_{0.8}Cu_{0.2}O$ particles. As for copper hydroxide, the two highest intense (−111) and (200) Bragg peaks characteristic of CuO, which are respectively located at $2\theta = 35.5°$ and 38.7°, are totally absent from the XRPD patterns of "hydroxylated nano-$Mg_{0.8}Cu_{0.2}O$ particles" (Fig. 5a). Whether $Cu(OH)_2$ or CuO, the corresponding particles probably have coherently diffracting domains so small in size that the associated Bragg peaks are too broad to clearly emerge from the background of XRPD patterns displayed in Fig. 5a.

C3-b. Hydration in static humid air atmosphere

Since the hydration kinetics of particles in moist air (80% RH) should be lower than in liquid water, the stability was monitored at 20 °C over a period as long as 35 days. The time evolution of XRPD patterns and IR spectra collected on the micrometer- and nanometer-sized particles of MgO and $Mg_{0.8}Cu_{0.2}O$ after their exposure to humid air are displayed in Fig. 6a and b, respectively.

For micro-MgO and micro-$Mg_{0.8}Cu_{0.2}O$ particles, no formation of a single $Mg(OH)_2$-type hydroxide is detected by XRPD even after 35 days of exposure to humid air (Fig. 6a). It is consistent with the absence of a stretching vibration band ν of hydroxyl group at around 3700 cm^{-1} in IR spectra collected over the same period (Fig. 6b). On the other hand, a very broad vibration band in the wavenumber region between 3800 and 2800 cm^{-1} and an intense band at ≈ 1425 cm^{-1} simultaneously appear in the IR spectra from the first day of exposure of both micro-MgO and micro-$Mg_{0.8}Cu_{0.2}O$ particles to humid air (Fig. 6b). As the days of exposure increase, these vibration bands still grow in intensity. The broad band is attributed to the elongation vibration of the O—H bonds within water molecules adsorbed at the surface of the oxide particles (ν_{H2O} in Fig. 6b). No vibration band for adsorbed CO_2 molecules is observed at 2350 cm^{-1} in IR spectra. Thereby, the intense band at $\approx$ 1425 cm^{-1} corresponds to the asymmetric stretching vibrations ν of C—O bonds in carbonate groups CO_3^{2-} **[30]** (ν_{CO3} in Fig. 6b). These carbonate groups come from the reactive adsorption of CO_2 molecules present in the humid air of the closed glass chamber onto the oxide surface. The asymmetric stretching vibration ν of C—O bonds in the free CO_3^{2-} ion (D_{3h} symmetry) gives rise to one active IR band at 1415 cm^{-1} **[38]**. These carbonate groups can be mono- or bi-coordinated to terminal divalent cations at the surface of MgO and $Mg_{0.8}Cu_{0.2}O$ particles [38]. Whatever the coordination of those adsorbed carbonate groups, their three C—O bonds are no more equivalent as in the free CO_3^{2-} ion. Thus, the IR band of the free CO_3^{2-} ion at 1415 cm^{-1} splits into two bands. The difference $\Delta\nu$ in position of these two bands can be as high as 100 cm^{-1} for a mono-coordination and 300 cm^{-1} for a bi-coordination of CO_3^{2-} ions [38]. In Fig. 6b, no splitting is observed except that, the intense band at ≈ 1425 cm^{-1} is asymmetric at high wavenumbers side. This asymmetry results from a strong overlapping of the two ν vibration bands with a difference $\Delta\nu$ not exceeding 80 cm^{-1}. One can thereby conclude that the carbonate groups are mono-coordinated to terminal divalent cations (Mg and Mg/Cu) at the surface of MgO and $Mg_{0.8}Cu_{0.2}O$ particles. Despite the simultaneous hydration and carbonation of particle surface for both micro-oxides, no carbonate and hydrated phase are detected by XRPD, even at trace level, under the data collection conditions used (Section 1.1 in Appendix A). Torres-Rodríguez et al. **[39]** showed that MgO particles exposed to wet CO_2 gas at 40 °C absorb by weight four times more H_2O and CO_2 molecules in 70% RH atmosphere (total of $\approx$ 16 wt%) than in 40% RH one (total of $\approx$ 4 wt%). Highfield et al. **[40]** demonstrated that more than 60 wt% of $MgCO_3$ are formed when microparticles of MgO (< 44 µm) are annealed above 300 °C under carbon dioxide partial pressure $P(CO_2)$ and steam greater than 20 bars and 5%vol, respectively. Both studies explain why under the temperature (20 °C) and RH (80%) conditions we used, only a surface carbonation of oxide particles occurs without detecting any $MgCO_3$ formed by XRPD.

Due to the large reactive surface available in the nanometer-sized particles, the sorption of H_2O molecules on their surface, as well as their carbonation, are kinetically faster than in the case of the micrometer ones (Fig. 6b). Indeed, the IR spectra show that the associated ν_{H2O} and ν_{CO3} bands for the nano-MgO and nano-$Mg_{0.8}Cu_{0.2}O$ particles exposed for 1 day have almost the same intensity as those observed for their micro-counterparts exposed for 35 days. Once the nanoparticle surface is carbonated in the early 10 days of exposure to humid air (Fig. 6b), the ν_{CO3} band no longer grows in intensity for both nano-oxides studied (Fig. 6b). Despite this surface carbonation of particles, no metal carbonate is detected by XRPD for both nano-oxides (Fig. 6a) under the data collection conditions used (Section 1.1 in Appendix A). In addition to the broad ν_{H2O} band, a narrow band appears at around 3700 cm^{-1} in the IR spectra of the nano-MgO and nano-$Mg_{0.8}Cu_{0.2}O$ particles from the first day of their exposure to humid air (Fig. 6b). From the hydration experiments carried out in liquid water (Fig. 5b), this band is ascribed to the stretching vibration ν_{OH} of hydroxyl group in a $Mg(OH)_2$-type hydroxide. The adsorption of H_2O molecules together with a weak surface hydroxylation of the MgO nanoparticles is fully supported by Newberg et al. study **[41]**. These authors investigated the reaction of water vapor with a MgO thin film using ambient pressure X-ray photoelectron spectroscopy. This study clearly shows that one monolayer of molecularly adsorbed water ($\approx$ 31 Å in thickness) interacts with a fully hydroxylated interface ($\approx$ 48 Å in thickness) on MgO thin film exposed to RH as low as 20% at room temperature. Adsorption of water and hydroxylation of MgO are obviously more important when relative humidity reaches 80%, thus allowing their easy detection by IR spectroscopy as in the present study (Fig. 6b). Although the IR spectra of the nano-$Mg_{0.8}Cu_{0.2}O$ particles are similar to that of nano-MgO ones, the XRPD patterns displayed in Fig. 6a reveal that the oxides behave differently when exposed to humid air. From the first day of exposure, a partial formation of $Mg(OH)_2$ is already noted for nano-MgO oxide whereas only a broadening and decrease in intensity of all Bragg peaks of $Mg_{0.8}Cu_{0.2}O$ oxide occur. Note that, the Bragg peaks are much wider for $Mg(OH)_2$ formed onto nano-MgO particles in humid air (Fig. 6a) than that produced on the same particles in liquid water (Fig. 5a). In the conventional view of the water vapor-MgO particle interaction **[42]**, water molecules first diffuse from the outer particle surface and then react to form a hydroxide shell around an oxide core. With exposure time, the hydroxide shell grows in thickness as the chemical reaction interface progresses to the particle core. This description is similar to that proposed for the reduction of metal oxide particles by gaseous dihydrogen **[43,44]**. In the early stages, the rate of $Mg(OH)_2$ formation is slow and strongly dependent on the reaction surface (*i.e.* the specific surface area). In Fig. 6b, no formation of by-product $Mg(OH)_2$ on the micrometer-sized MgO particles occurs within the first 35 days of

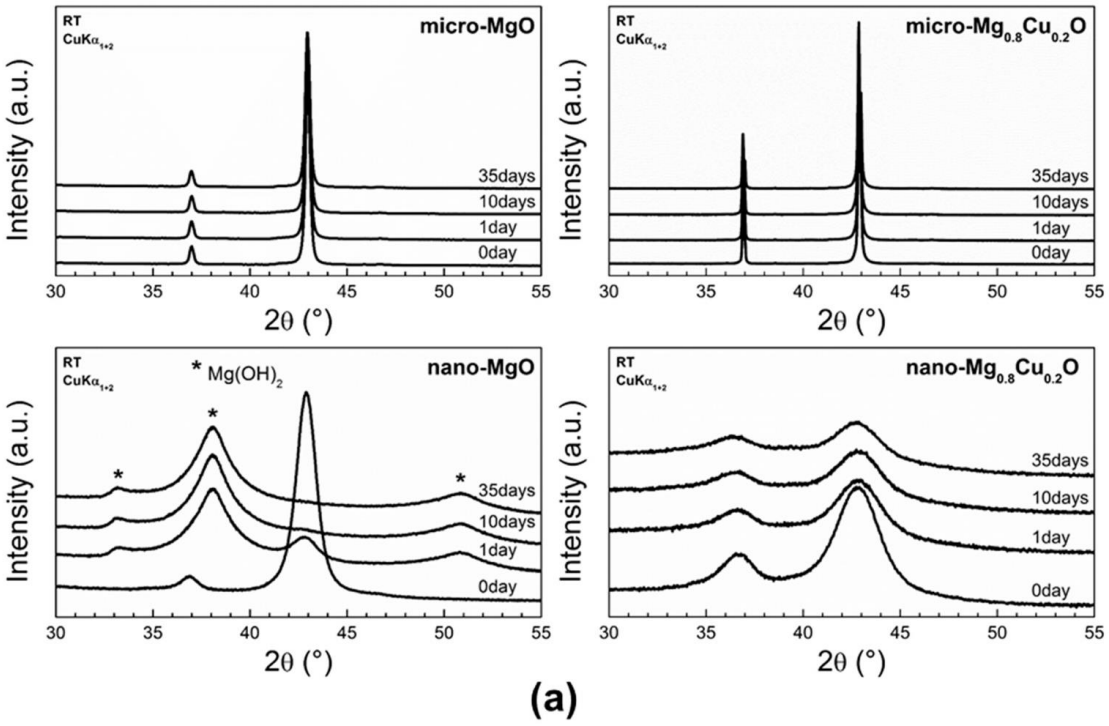

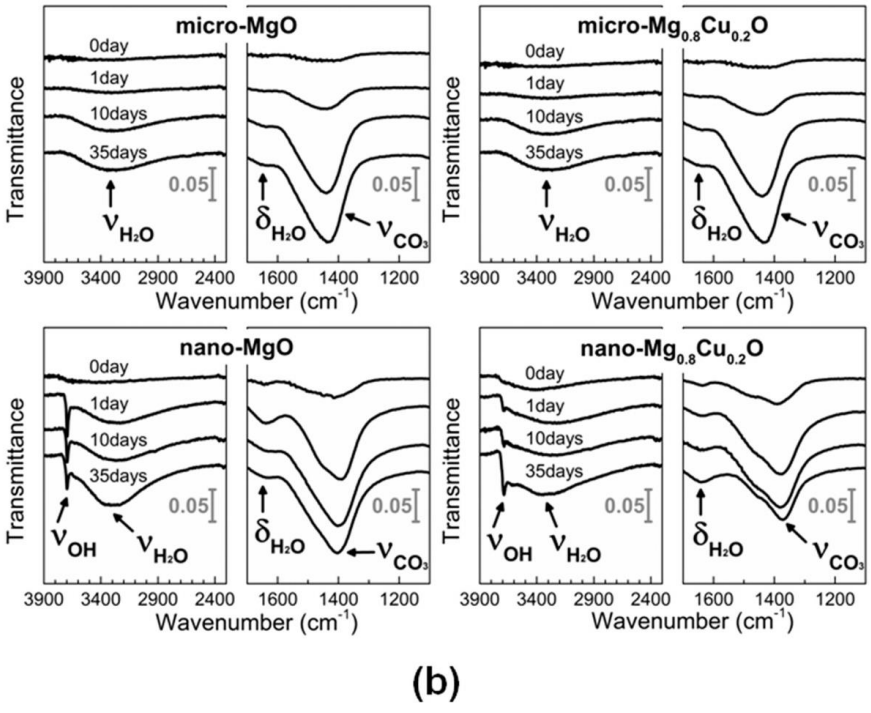

Fig. 6. Evolution of XRPD patterns (a) and IR transmission spectra (b) collected *ex-situ* and at room temperature (RT) on the micrometer- and nanometer-sized particles of MgO and $Mg_{0.8}Cu_{0.2}O$ after specified days of exposure to static humid air atmosphere (80% RH).

exposure to humid air due the small reactive surface available (thus meaning that the induction period is longer than 35 days). In the course of the hydroxylation process from the water vapor, the 3D long range order initially existing in well-crystallized oxide particles can be partially or even totally lost, especially, when the hydroxylation reaction involves moving from a 3D cubic NaCl-type structure for MgO to a hexagonal layered structure for $Mg(OH)_2$. At high hydroxylation rate, the XRPD pattern of the resulting hydroxide can show either wide Bragg peaks (poorly-crystallized state) or very weak undulation of the background (amorphous state). The situation is very different in liquid water because $Mg(OH)_2$ only precipitates if a dissolution of terminal Mg^{2+}/OH^- at the surface of MgO particles beforehand occurs, such as when adding an alkaline solution dropwise to a magnesium salt solution. During the nucleation stage in liquid water, (Mg^{2+}/OH^-) ions perfectly order over long range in the crystal structure of the by-product hydroxide. Thus, the XRPD pattern of $Mg(OH)_2$ precipitated in water shows narrow Bragg peaks such as those displayed in Fig. 5a (or in the XRPD pattern of $Mg(OH)_2$ particles obtained by precipitation route in reference [14]). Now, to be consistent with both the presence of ν_{OH} band in IR spectra (Fig. 6b) and the absence of crystallized hydroxide in XRPD pattern (Fig. 6a), the copper-containing particles must have an amorphous $Mg_{1-x}Cu_x(OH)_2$ shell around an oxide core. This oxide core having a size smaller than that of the initial oxide particle, the $Mg_{0.8}Cu_{0.2}O$ diffraction peaks broaden with hydroxylation (Fig. 6a). Because long-range ordered or crystallized $Mg(OH)_2$ is detected by XRPD for the exposed nano-MgO particles, copper is responsible for the amorphization of the hydroxide shell formed around the nano-$Mg_{0.8}Cu_{0.2}O$ core. Ten days of exposure to humid air are sufficient for the complete conversion of nano-MgO into magnesium hydroxide. For the nano-$Mg_{0.8}Cu_{0.2}O$ particles, neither crystallization of the amorphous $Mg_{1-x}Cu_x(OH)_2$ shell nor complete conversion of the oxide core has even been detected by XRPD after 35 days of exposure (Fig. 6a). Thereby, the copper-substituted MgO nanoparticles surprisingly exhibit a resistance to complete hydroxylation with water vapor at least for the first month of their exposure.

In Fig. 2b, no trace of hydroxide is detected in the XRPD patterns collected on the micro- and nano-$Mg_{1-x}Cu_xO$ particles at ambient air atmosphere (60% RH) and temperature. As shown in Fig. 6, no hydroxylation of microparticles is detected after the first day of their exposure to humid air atmosphere with high RH (80%). In that way, the cell parameters a of the different micro-$Mg_{1-x}Cu_xO$ samples determined at ambient air and lower RH (60%) are those of microparticles free of hydroxide shell. The situation could be however different for nanoparticles under 60% RH since they are highly sensitive to water vapor on the first day of exposure, as shown in Fig. 6. In Fig. 3, a constant $\approx +0.24\%$ expansion of the parameter a is noticed for each composition of the solid solution $Mg_{1-x}Cu_xO$ when nano-structuring the particles. From the crystal structure of MgO shown in Fig. 1a, the shortest Mg—Mg distance corresponds to $d = a\sqrt{2}/2$ with a the cubic cell parameter. Thus, the nano-structuring involves a lengthening of the (Mg,Cu)-(Mg,Cu) distance d by $\approx +0.24\%$. In brucite-type $Mg_{1-x}Cu_x(OH)_{2-2y}(CO_3)_y$ hydroxides [14], the shortest (Mg,Cu)-(Mg,Cu) distance corresponds to the hexagonal cell parameter a which stays at around 3.15 Å whatever x. On average, the (Mg,Cu)-(Mg,Cu) distance d in mixed hydroxides is therefore $\approx 5\%$ longer than that of in mixed oxides. The lengthening of the (Mg,Cu)-(Mg,Cu) distance in $Mg_{1-x}Cu_xO$ nanoparticles is therefore consistent with their weak hydroxylation. The numerous defects present in nanoparticles (Section 3.2) favour the sorption of water molecules. The hydroxylation rate (kinetics) of all $Mg_{1-x}Cu_xO$ nanoparticles should be very similar because the defect density (lattice strain of $\approx +0.4\%$ in average, Fig. 3) and the lengthening rate of d ($\approx +0.24\%$, Fig. 3) are both invariant to the copper content x in the series. Despite the XRPD patterns are recorded shortly after their synthesis and the sample preparation for the measurements, the formation of the hydroxide shell onto the surface of the nano-$Mg_{1-x}Cu_xO$ particles cannot be avoided at ambient air (60% RH). For the nano-MgO particles, the presence of the hydroxide shell is impossible to detect by XRPD as long as its thickness is small and the time of exposure is short. It is even more difficult for copper substituted nanoparticles because no long-range ordered hydroxide phase is formed even after the first month of their exposure to humid air. In that way, the linear dependence of the cubic cell a parameter on the copper content x in the nano-$Mg_{1-x}Cu_xO$ series (Fig. 3) refers to particles covered with a very thin and coherent hydroxide shell.

C4. Bactericidal activity

In 2005, Makhluf et al. [3] greatly enhanced the bactericidal kinetics of MgO particles towards *S. aureus* and *E. coli* by reducing their size down to 23 nm. The reductions in viability of both bacteria are greater than 95% (> 1 Log_{10}) after 4 h (240 min) in contact with a suspension in particles at 1 $mg.mL^{-1}$ whose size is around 8 ± 1 nm. Nguyen et al. [45] determined that 1 $mg.mL^{-1}$ is the minimal concentration in nano-MgO particles ($Ø \approx 23 \pm 5$ nm) inducing a 99.9% (3 Log_{10}) reduction in viability of both *E. coli* and *S. aureus* after 24 h (1440 min) in contact. In the present study and for comparison purposes, the concentration of particles within the suspension of bacteria was 1 $mg.mL^{-1}$, which is identical to the one chosen by Makhluf et al. [3] and Nguyen et al. [45]. However, we have evaluated the bactericidal activities of both micrometer- and nanometer-sized $Mg_{1-x}Cu_xO$ particles in sterile distilled water rather than in a mixture of nutrient and physiological buffer media, as done in the cited studies (NaCl solution with Luria Bertani Broth (LBB) in the former [3] or Tris buffer with Luria Bertani Broth (LBB) and Tryptic Soy Broth (TSB) in the latter [45]). The reason is that the peptones or tryptones, a mixture of polypeptides and amino acids, present in these culture media can interact with studied particles, thus affecting and preventing to determine their intrinsic bactericidal performances. Indeed, Makhluf et al. [3] have observed that the bactericidal performance of MgO nanoparticles in nutrient LBB medium is almost twice lower than that in medium free of peptones. They have postulated that the direct interaction of MgO nanoparticles with those peptones prevents the adsorption of the particles onto the cell envelopes. In fact, less MgO nanoparticles are effectively adsorbed onto the cell envelopes because they dissolve in the LBB medium with time, as evidenced by Wetteland et al. [46] (more than 39 mol% of nanoparticles at initial concentration of 1 $mg.mL^{-1}$ are dissolved in 24 h; *i.e.* $\approx 1 \times 10^{-2}$ $mol.L^{-1}$ of solvated Mg^{2+}). This dissolution rate in 24 h is even higher for the TSB medium (more than 49 mol% of MgO nanoparticles at initial concentration of 1 $mg.mL^{-1}$; *i.e.* $\approx 1.2 \times 10^{-2}$ $mol.L^{-1}$ of solvated Mg^{2+}). In addition, the same authors demonstrated that *E. coli* is not sensitive to any increase in concentration of solvated Mg^{2+} ions up to 5×10^{-2} $mol.L^{-1}$ [46] because those ions cannot catalyse the production of Reactive Oxygen Species (ROS) as MgO nanoparticles do [47]. Gunawan et al. [48] showed that the free amino acids in LBB culture medium also promote the dissolution of CuO nanoparticles. The possibility for terminal and sub-coordinated cupric ions at the surface of those CuO nanoparticles to complete their coordination with amino acids is certainly the initial step leading to the release of Cu^{2+} in the medium. However, no lysis of *E. coli* cells is observed because peptides present in the LBB medium form no toxic complexes with cupric ions thus released, which considerably reduces the amount and cytotoxic effect of free Cu^{2+} on bacteria. These findings well support those of Menkissoglu et al. [49] who demonstrated that the Gram-negative *P. syringae* in a culture medium rich in casitones is resistant to treatments with copper sulphate even at relatively high concentration because more than 99% of Cu^{2+} species form no toxic complexes with those peptones. In addition, chloride ions are systematically present in physiological buffer media such as PBS, Tris-Cl or DMEM. As reported by Wetteland et al. [50], their presence is responsible for the complete dissolution of MgO and $Mg(OH)_2$ nanoparticles after 24 h of immersion in DMEM at 1 $mg.mL^{-1}$. Weak dissolution of CuO is also noted in PBS or Tris-Cl buffer media [51]. Note that, proteins/peptides/amino acids and chloride ions are not simultaneously present in the vicinity of the

bactericidal agents when used to fight infections in real life. Their impact on the bactericidal activity of $Mg_{1-x}Cu_xO$ particles being out of the scope of the current study, it will not thereby be investigated.

For each mixed oxide tested in both micro- and nano-$Mg_{1-x}Cu_xO$ series, the sterile water suspension of particles in contact with a bacterial strain (final concentration at $\approx 10^6$ CFU.mL^{-1}) was maintained at 20 °C for 15, 30, 60 and 180 min under controlled shaking speed. Sawai et al. **[52]** showed that 3.6 μm-sized MgO particles quickly settled at low shaking speed of the suspension thus decreasing their bactericidal activity against *E. coli*. In the present study, a shaking speed of 250 shakes per min was selected to prevent sedimentation of particles. The evaluation of bactericidal activity was conducted at 20 °C rather than 37 °C as in the JISZ 2801 test conditions because this is the temperature typical of indoor environments such as hospitals. After each contact time t, a counting of the number N_t of CFU was performed to estimate the reduction in cell viability. For both *E. coli* and *S. aureus*, the number N_t of CFU at the different time in contact with micrometer- and nanometer-sized particles of $Mg_{1-x}Cu_xO$ are respectively displayed as a function of the copper content x in Tables S3 and S4 in Appendix A.

For micrometer-sized $Mg_{1-x}Cu_xO$ particles, all copper containing oxides exhibit a reduction in viability of *E. coli* greater than 60% after the first 30 min (Table S3). Such a level of reduction is not even reached by microparticles of the parent oxide MgO after 180 min. Although the copper substitution greatly enhances the bactericidal activity of MgO microparticles, the suspension under test is not completely free of *E. coli* when treated with copper-substituted counterparts for 180 min since the Log_{10} reduction does not exceed 4.5 for the most active composition $x = 0.05$. A lowering of the bactericidal kinetics is surprisingly noticed as the copper content x increases in the micrometer-sized particles. Despite its low copper content, the $Mg_{0.95}Cu_{0.05}O$ sample therefore combines both the highest level of reduction in viability and the fastest bactericidal kinetics compared to others (Table S3). The beneficial effect of the copper substitution on the level of bactericidal activity of micro-MgO is much pronounced towards *S. aureus* than towards *E. coli*, the kinetics being very similar for the activity of a given sample towards both bacteria (Table S3). In the SEM images displayed in Fig. S2, (Section 3 in Appendix A), a dispersity in the size of microparticules exists within the same sample. For a given sample, this varying size of microparticles affects their interaction with the cell envelopes and thereby their ability to kill bacteria. It may explain why the complete eradication of both bacteria is never reached after 180 min of treatment with those microparticles whatever their copper content. Sometimes, the reduction in viability of *E. coli* or *S. aureus* at a specified time can significantly differ from the first assay to the second one for a selected composition, thus making large in magnitude the associated standard deviations on the number of CFU (Table S3). To our opinion, the large standard deviations reflect that activity is very sensitive to the fraction of small microparticles in the suspension, a parameter that may vary between assays.

For nanometer-sized particles of $Mg_{1-x}Cu_xO$, all copper containing oxides exhibit a reduction in viability of *E. coli* greater than 99.9% (> 3 Log_{10}) after the first 30 min and kill the entire initial inoculum after 180 min (> 6.5 Log_{10} in Table S4). This exceptionally high level of activity towards *E. coli* is even reached after 30 min and 60 min for the $x = 0.1$ and $x = 0.05$ samples, respectively. The $Mg_{0.9}Cu_{0.1}O$ sample therefore combines both the highest level of reduction in viability of *E. coli* and the fastest bactericidal kinetics compared to others (Table S4). Once again, it demonstrates that the bactericidal performance is not proportional to the copper content of nanoparticles. The nano-structuring of particles is also beneficial to the parent compound MgO which now displays a 4 Log_{10} reduction in viability of *E. coli*. Such a reduction towards *E. coli* is higher than the one reported by Makhluf et al. **[3]** after 240 min of treatment with a suspension at 1 mg.mL^{-1} in nanoparticles of MgO whose size is around 8 ± 1 nm (≈ 3 Log_{10}). The nano-structuring of $Mg_{1-x}Cu_xO$ particles has also a beneficial effect on the bactericidal activity towards *S. aureus* even if it is of smaller amplitude (Tables S3 and S4). For both bacteria, the standard deviations on the counts of viable cell are however significantly lower for nanoparticles than those reported for microparticles. This trend is especially pronounced for *S. aureus*. Nguyen et al. **[45]** and Halbus et al. **[6]** have, respectively, measured the zeta potential of nanoparticles of MgO (+32.31 ± 4.1 mV) and CuO (+30 mV) in water. These values are very similar. Thereby, copper substitution cannot significantly change the zeta potential of the parent MgO oxide. This indicates that $Mg_{1-x}Cu_xO$ nanoparticles can be adsorbed onto the negatively charged membrane of cells thanks to electrostatic interactions. Thus, the reduction in size of particles greatly improves their mass adsorption onto the cell envelopes and their ability to rapidly kill bacteria in a reproducible manner between assays.

The bactericidal performances of nanometer-sized particles of the mixed oxides $Mg_{1-x}Cu_xO$ ($0 \leq x \leq 0.2$) are then compared with those of the conventional inorganic antibacterial agent CuO. For this purpose, the bactericidal activity of CuO particles has been determined in conditions similar to those used for the mixed oxides studied (1 mg.mL^{-1}) and with particles of comparable size. 50 nm-sized CuO particles were synthesized by thermally decomposing nanometer-sized $Cu(OH)_2$ particles. The copper hydroxide was prepared beforehand by the same synthetic route used for mixed hydroxides from which the $Mg_{1-x}Cu_xO$ nanoparticles were obtained. The reductions in viability of *E. coli* and *S. aureus* at the different specified times in contact with those CuO nanoparticles were tabulated in reference **[14]**. The time dependence of the Log_{10} reduction in viability of both bacteria is displayed in Fig. 7 as a function of the copper content x in the nano-$Mg_{1-x}Cu_xO$ particles and then compared with those of nano-CuO. At first, the reductions in viability of *E. coli* with those 50 nm-sized particles of CuO are in the range 2 to 3 Log_{10} at contact times shorter than 60 min, which is lower than those with all nano-$Mg_{1-x}Cu_xO$ particles whatever their copper content x (Fig. 7). At both $t = 30$ min and 60 min, the counts of *E. coli* killed with 50 nm-sized particles of CuO even remain 3 orders of magnitude lower than those with the most active $Mg_{0.9}Cu_{0.1}O$ nanoparticles. After 180 min in contact with CuO nanoparticles, the reduction in viability does not exceed 4.7 Log_{10} which is still far lower than the 6.5 Log_{10} reductions determined with all copper-substituted MgO nanoparticles at the same specified time (*i.e.* $x = 0.05$ to 0.2 samples in Table S4 and Fig. 7). Secondly, the reduction in viability of *S. aureus* is lower than 0.1 Log_{10} (< 20%) after 60 min and finally rises to 2 Log_{10} (99%) after 180 min in contact with 50 nm-sized CuO particles. As shown in Fig. 7, all copper-substituted MgO nanoparticles kill more than 70% of the *S. aureus* inoculum after 60 min (> 0.7 Log_{10}). After 180 min, the reductions in viability overtake 2.6 and 3.6 Log_{10} for the $Mg_{0.9}Cu_{0.1}O$ and $Mg_{0.85}Cu_{0.15}O$ nanoparticles, respectively. From all the above results, only 10 mol% of cupric ions in MgO nanoparticles are sufficient to kill both the Gram-positive and Gram-negative bacteria with a kinetics faster and a level higher than the conventional CuO nanoparticles (Fig. 7). The use of 10 mol% copper substituted MgO nanoparticles as bactericidal agent in lieu of CuO gives the opportunity to 5.5-fold reduce the copper loading needed to kill all bacteria in the water suspension (Cu loading of 0.799 mg.mL^{-1} and 0.144 mg.mL^{-1} in the suspension of CuO and $Mg_{0.9}Cu_{0.1}O$ nanoparticles at 1 mg.mL^{-1}, respectively). This is a significant step towards the design of more environmentally friendly bactericidal agents than the ecotoxic cupric oxide.

C5. Bactericidal mechanism

Sawai et al. **[53]** considered that the alkaline effect caused by the hydration of MgO is one of the contributing factors to its bactericidal activity against eukaryotic cells like yeasts (*Saccharomyces cerevisiae* and *Candida albicans*) and filamentous fungi (*Aspergillus niger* and *Rhizopus stolonifer*). Mendonca et al. **[54]** showed that the reduction in viability was around 8 Log_{10} after only 15 min in contact with a sterile $NaHCO_3$-NaOH buffer at pH = 11 while it was only 0.5 Log_{10} at pH = 10. As stated in Section 3.3.1, when nano-MgO particles are immersed in liquid water for 180 min, the pH of the supernatant is slightly above 10 (Table 1) and

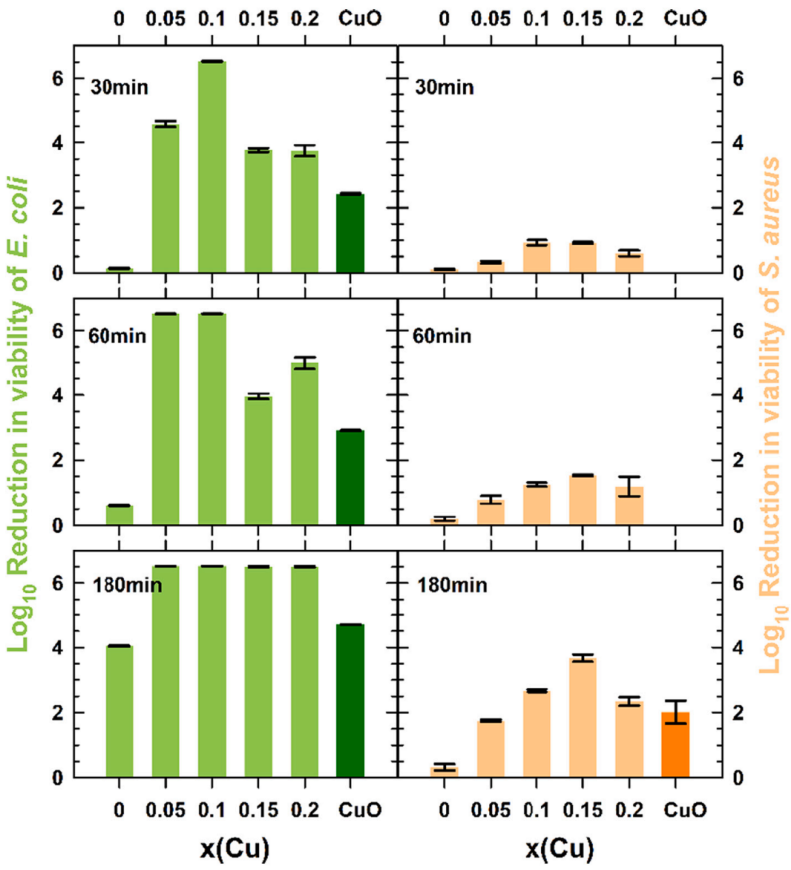

Fig. 7. Time dependence of the reduction in viability of *E. coli* and *S. aureus* in contact with nanometer-sized $Mg_{1-x}Cu_xO$ particles with different copper content x (Log_{10} average value±standard deviation over 2 assays). The bactericidal activity of 50 nm-sized CuO particles determined in the same conditions was extracted from reference [14].

the hydroxylation rate reaches ≈ 91% (Fig. 5c). In a previous study [14], we have demonstrated that the reductions in viability of *E. coli* and *S. aureus* in contact with platelet-like particles of $Mg(OH)_2$ (≈ 20 nm in diameter and ≈ 7 nm in thickness) for 180 min were as low as or even lower than 0.3 Log_{10} despite a pH of the supernatant close to 11. It is therefore surprising in this case to notice that "hydroxylated"-MgO nanoparticles induce a reduction in viability of *E. coli* as high as 4 Log_{10} after 180 min (Table S4) at pH ≈ 10 (Table 1). These two results clearly show that the high lethality of *E. coli* cannot be ascribed to any alkaline effect of the water suspension of "hydroxylated"-MgO nanoparticles. The only explanation for the high level of activity is that the 12 nm-sized $Mg(OH)_2$ particles *in-situ* produced from the dissolution of nano-MgO (see Section 3.3.1) are rapidly mass adsorbed onto the cell envelopes as soon as they precipitate. The adsorption of the *in-situ* produced Mg $(OH)_2$ nanoparticles is also better than those beforehand synthesized because they are smaller in size (12 nm *versus* 20 nm). Since dissolution of MgO particles is size-dependent (Fig. 5, Table 1 and Fig. 6), the same is true for their bactericidal performances (Tables S3 and S4). Indeed, the hydroxylation rate α of MgO at $t = 180$ min is as low as ≈ 14% for microparticles and rises to ≈ 91% for nanoparticles (Fig. 5c). At the same time, the reduction in viability of *E. coli* jumps from 0.3 Log_{10} to 4 Log_{10} by reducing the particle size of MgO. The smaller the particle size, the faster the particles dissolve in liquid water and the larger the amount of $Mg(OH)_2$ produced/adsorbed onto the cell envelopes. This finding is consistent with Makhluf et al. [3] study showing that reductions in viability of both bacteria can be doubled after 4 h (240 min) of treatment by decreasing the size of MgO particles from 23 nm (< 40%) to 8 nm (> 95%). Wetteland et al. [46] showed that the viability of *E. coli* is in no way affected by any increase in concentration of solvated Mg^{2+} ions up to 5×10^{-2} mol.L^{-1} (*i.e.* 1215 mg.L^{-1}). Since the concentration in Mg^{2+} released in the supernatant by the dissolution of MgO nanoparticles is only around 6.1 mg.L^{-1} at 180 min (Table 1), the solvated Mg^{2+} ions have no contribution to the bactericidal activity towards *E. coli*. and very likely towards *S. aureus* as well. It demonstrates that $Mg(OH)_2$ is the active phase.

Although no formation of hydroxide occurs even after 960 min of immersion of the micrometer-sized $Mg_{0.8}Cu_{0.2}O$ particles in liquid water (Fig. 5a), reductions in viability of *E. coli* and *S. aureus* greater than 3.8 Log_{10} are nevertheless achieved at 180 min. Unlike the parent compound MgO, the microparticles of $Mg_{1-x}Cu_xO$ have an intrinsic bactericidal power ascribed to the presence of cupric ions (ROS production). In our previous study [14], we have demonstrated that regardless the copper content in nanoparticles of $Mg_{1-x}Cu_x(OH)_2$, the reductions in viability of *E. coli* and *S. aureus* were greater than 6 Log_{10} and around 2 Log_{10} after 180 min of treatment, respectively. While the pH of the supernatant is just below 10 (Table 1), the same levels of bactericidal activity are also reached after 180 min of treatment with all $Mg_{1-x}Cu_xO$ nanoparticles (Fig. 7). The minimal inhibitory concentrations (MIC) in soluble cupric ions for the growth of *E. coli* and *S. aureus* are 25 mg.L^{-1} and 12.5 mg.L^{-1}, respectively [55]. For $Mg_{0.8}Cu_{0.2}O$ nanoparticles,

neither the concentration of 0.3 mg.L^{-1} in cupric ions nor the concentration of 7.5 mg.L^{-1} in Mg^{2+} in the water suspension at 180 min (Table 1) have therefore any bactericidal effect on *E. coli* and very likely on *S. aureus* as well. When $Mg_{0.8}Cu_{0.2}O$ nanoparticles dissolve in liquid water, a concomitant precipitation of copper hydroxide is suspected (Section 3.3.1). Akhavan et al. **[56]** have demonstrated that copper hydroxide exhibits bactericidal activity. But, the minute amount of Cu $(OH)_2$ nanoparticles in the water suspension of $Mg_{0.8}Cu_{0.2}O$ nanoparticles makes its contribution to their lethal activity insignificant. At time shorter than 180 min, both $Mg_{1-x}Cu_xO$ and $Mg_{1-x}Cu_x(OH)_2$ nanoparticles coexist in water suspension as evidenced by diffraction for the x = 0.2 sample in Fig. 5a. Since $Mg_{1-x}Cu_xO$ microparticles have an intrinsic bactericidal activity, the same must be true for the corresponding nanoparticles. Thereby, $Mg_{1-x}Cu_x(OH)_2$ nanoparticles formed *in-situ* in the water suspension of bacteria together with the undissolved $Mg_{1-x}Cu_xO$ nanoparticles contribute to the bactericidal activities reported in Table S4 at time shorter than 180 min. At 180 min, the bactericidal performances can be assigned to the $Mg_{1-x}Cu_x(OH)_2$ nanoparticles alone. In our previous study on the bactericidal activity of $Mg_{1-x}Cu_x(OH)_2$ nanoparticles [14], 15 mol% copper-substituted $Mg(OH)_2$ was the single mixed hydroxide exhibiting the fastest bactericidal kinetics and the highest reductions in viability towards both bacteria whereas the 10 mol% copper-substituted MgO oxide meets these features over the same 180-min period (*i.e.* $Mg_{0.9}Cu_{0.1}O$ in Fig. 7). The reason is simple: the speed at which $Mg_{1-x}Cu_x(OH)_2$ nanoparticles precipitate decreases as the copper content increases while the higher the copper content of the $Mg_{1-x}Cu_x(OH)_2$ nanoparticles the greater their bactericidal activity. The best balance between those two antagonistic effects is reached for a 10 mol% copper content in MgO nanoparticles.

Sawai et al. **[47]** and later Makhluf et al. **[3]** have determined the bactericidal mechanism of nanometer-sized MgO particles, (which must be definitively considered as quickly or fully converted into $Mg(OH)_2$ from the present study). The mechanism would result from the following successive actions: i) generation of exogenous reactive oxygen species (*e.g.* free $HO^\bullet$ and $O_2^{\bullet-}$ radicals) by the particles attached to the bacterial cell membrane, ii) increase in permeability of the cell envelope due to the damage induced by exogenous ROS, iii) penetration of individual particles into the cell and iv) cell lysis with loss of vital intracellular content (DNA and RNA) damaged by endogenous ROS generation. Consequently, electron paramagnetic resonance (EPR) was used to track ROS produced in water suspensions of MgO and $Mg_{0.9}Cu_{0.1}O$ nanoparticles as well as their "hydroxylated" analogues $Mg(OH)_2$ and $Mg_{0.9}Cu_{0.1}(OH)_2$ (synthesized as in reference **[14]**) at the same concentration (1 mg.mL^{-1}) as used in the bactericidal tests. To support the presented assumptions on the major role played by the hydroxides in the bactericidal activity reported for the oxides, the EPR spin trapping experiments were performed for the oxide and hydroxide both having the same copper content (x = 0 or 0.1). Spin trapping technique provides the possibility to monitor and identify reactive radical intermediates, as $O_2^{\bullet-}/HO_2^\bullet$ and $HO^\bullet$, by their addition to a diamagnetic spin trap molecule (*i.e.* 5,5-dimethyl-1-pyrroline *N*-oxide, DMPO) to form a more stable radical-adduct detectable by EPR.

No EPR signals were monitored in the aerated water suspensions of MgO or $Mg(OH)_2$ nanoparticles in the presence of DMPO spin trapping agent. However, a low-intensity six-line EPR signal was measured for both aerated water suspensions of $Mg_{0.9}Cu_{0.1}O$ and $Mg_{0.9}Cu_{0.1}(OH)_2$ nanoparticles containing DMPO (Fig. S3, Section 5 in Appendix A), with hyperfine coupling constants characteristic for the DMPO spin-adduct of a carbon-centered radical ($a_N = 1.585 \pm 0.003$ mT, $a_H^\beta = 2.300 \pm 0.005$ mT; $g = 2.0055$). As DMPO represents the only source of carbon in this experimental system, we supposed that the production of carbon-centered radical (and its corresponding DMPO-adduct) results from the decomposition of DMPO in alkaline media in the presence of Cu^{2+} ions.

It is well known that alkaline media **[57–60]** can promote the decomposition of hydrogen peroxide into reactive oxygen species, *i.e.* $O_2^{\bullet-}/HO_2^\bullet$ and $HO^\bullet$ (Eqs. (1)–(4)). In addition, cupric ions can catalyse the generation of ROS from aqueous H_2O_2 through a Fenton-like redox cycling between Cu^{2+} and Cu^+/Cu^{3+} ions **[61,62]** (Eqs. (5)–(9)).

$$HO_2^\bullet \Leftrightarrow O_2^{\bullet-} + H^+ \quad (1)$$

$$H_2O_2 + OH^- \Leftrightarrow HO_2^- + H_2O \quad (2)$$

$$H_2O_2 + HO_2^- \rightarrow O_2^{\bullet-} + HO^\bullet + H_2O \quad (3)$$

$$HO^\bullet + H_2O_2 \rightarrow HO_2^\bullet + H_2O \quad (4)$$

$$Cu^{2+} + H_2O_2 \rightarrow Cu^+ + O_2^{\bullet-} + 2H^+ \quad (5)$$

$$Cu^+ + H_2O_2 \rightarrow Cu^{2+} + OH^- + HO^\bullet \quad (6)$$

$$Cu^+ + H_2O_2 \rightarrow Cu^{3+} + 2OH^- \quad (7)$$

$$Cu^{3+} + H_2O_2 \rightarrow Cu^{2+} + O_2^{\bullet-} + 2H^+ \quad (8)$$

$$Cu^{2+} + O_2^{\bullet-} \rightarrow Cu^+ + O_2 \quad (9)$$

Hydrogen peroxide is a by-product of the normal metabolism of oxygen in aerobically living organisms **[63]** and is present at millimolar concentration in the culture supernatant of *E. coli* and *S. aureus* **[64]** despite their catalase activity. Thus, the presence of hydrogen peroxide in the medium could play a crucial role in the bactericidal mechanism of the nanoparticles studied. Consequently, H_2O_2 was added to all aerated water suspensions of nanoparticles containing DMPO and the EPR spectra were recorded under the same conditions as above. Aqueous suspensions of MgO and $Mg(OH)_2$ nanoparticles containing H_2O_2 and DMPO exhibit EPR spectra similar to those of their copper containing analogues (Fig. 8). Each experimental EPR spectrum can be satisfactorily fitted with two superimposed signals characterized by the spin-Hamiltonian parameters typical for two DMPO-adducts of oxygen-centered radicals, namely $^\bullet$DMPO-O_2^-/O_2H (12-line signal; $a_N = 1.416 \pm 0.008$ mT, $a_H^\beta = 1.132 \pm 0.009$ mT, $a_H^\gamma = 0.140 \pm 0.019$ mT; $g = 2.0058$) and $^\bullet$DMPO-OH (4-line signal; $a_N = 1.504 \pm 0.004$ mT, $a_H^\beta = 1.471 \pm 0.001$ mT; $g = 2.0057$) **[65,66]** (Fig. 8). Since the water suspension of MgO and $Mg(OH)_2$ nanoparticles in the presence of H_2O_2 revealed the comparable ability to generate ROS as their copper-substituted counterparts, the main mechanism of the ROS generation is most likely coupled with the decomposition of hydrogen peroxide at the alkaline pH imposed by the dissolution of nanoparticles in water (pH values in Table 1 for MgO and $Mg_{0.9}Cu_{0.1}O$ and reference **[14]** for Mg $(OH)_2$ and $Mg_{0.9}Cu_{0.1}(OH)_2$).

The intensity of each EPR signal is strongly affected by: i) concentration/stability of original radical; ii) bimolecular rate constant for the addition of original radical to spin trap; iii) stability of the spin-adduct formed. For the $O_2^{\bullet-}/HO_2^\bullet$ trapping by DMPO, both the rate constant and the stability of spin-adducts are significantly dependent on pH values **[67,68]**. While the observed EPR signal of $^\bullet$DMPO-O_2^-/O_2H unambiguously evidences generation of $O_2^{\bullet-}/HO_2^\bullet$, the $^\bullet$DMPO-OH spin-adduct may originate from different sources, *e.g.* genuine addition of hydroxyl radicals from hydrogen peroxide (Eq. (3)), Fenton-like processes (Eq. (6)) to DMPO spin trap or the $^\bullet$DMPO-O_2^-/O_2H dismutation in aqueous media **[69,70]**. To confirm the intrinsic production of hydroxyl radicals following the interaction of the studied nanoparticles with hydrogen peroxide, the spin trapping experiments were further conducted in the presence of dimethyl sulfoxide (DMSO). While DMSO stabilizes free $O_2^{\bullet-}$ radicals in water **[69]**, it is extremely reactive towards free hydroxyl radicals by generating the carbon-centered radicals according to Eqs. (10) and (11).

$$DMSO + HO^\bullet \rightarrow {}^\bullet CH_3 + CH_3SO(OH) \quad (10)$$

$$DMSO + HO^\bullet \rightarrow H_2O + CH_3SOCH_2^\bullet \quad (11)$$

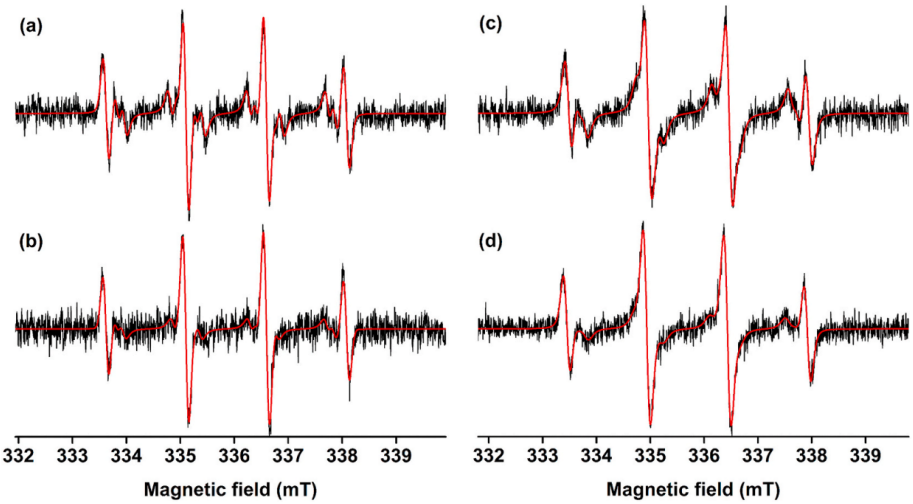

Fig. 8. Normalized experimental (black line) and simulated (red line) EPR spectra measured after the addition of hydrogen peroxide ($c_0(H_2O_2) = 0.03$ M) to the aerated water suspensions of studied nanoparticles (loading 1 mg.mL^{-1}) in the presence of DMPO spin trapping agent (c_0(DMPO) = 0.04 M). The relative concentration of $^{\bullet}$DMPO-OH and $^{\bullet}$DMPO-O_2^-/O_2H spin adducts evaluated from the simulated spectra are as follows: (a) MgO (44.2% and 55.8%); (b) $Mg(OH)_2$ (50.0% and 50.0%); (c) $Mg_{0.9}Cu_{0.1}O$ (51.9% and 48.1%) and (d) $Mg_{0.9}Cu_{0.1}(OH)_2$ (58.8% and 41.2%). (For interpretation of the references to color in this figure legend, the reader is referred to the web version of this article.)

$$^{\bullet}CH_3 + O_2 \rightarrow CH_3O_2^{\bullet} \quad (12)$$

$$CH_3SOCH_2^{\bullet} + O_2 \rightarrow CH_3SOCH_2O_2^{\bullet} \quad (13)$$

In the presence of dissolved molecular dioxygen, these carbon-centered radicals are readily transformed to peroxyl radicals (Eqs. (12) and (13)), which can be then trapped by DMPO as the corresponding alkoxy-radical spin-adducts ($^{\bullet}$DMPO-OCH_3 and $^{\bullet}$DMPO-OR with R = CH_3SOCH_2) [70]. No EPR signals were detected in the aerated DMSO/water (7/3; v:v) suspensions of MgO, $Mg(OH)_2$, $Mg_{0.9}Cu_{0.1}O$, and $Mg_{0.9}Cu_{0.1}(OH)_2$ in the presence of DMPO spin trapping agent. Only the addition of hydrogen peroxide to DMSO/water suspensions led to the detection of EPR signals. The corresponding spectra are complex and comparable for all oxides and hydroxides tested (Fig. S4, Section 5 in Appendix A). The thorough simulation analyses of these EPR spectra revealed the superimposition of four different DMPO spin-adducts with the spin-Hamiltonian parameters and relative concentrations summarized in Table S5. The detection of both methyl- and alkoxy-radicals clearly demonstrates that hydroxyl radicals are also produced by all nanoparticles tested. Consequently, it can be concluded that, the $^{\bullet}$DMPO-OH spin-adducts detected in water suspensions (Fig. 8) result from the trapping of free hydroxyl radicals intrinsically generated by all nanoparticles in the presence of H_2O_2.

According to Eq. (9), cupric ions are capable of converting superoxide radicals produced from H_2O_2 decomposition in alkaline media (Eq. (3)) and Fenton-type reaction (Eq. (5)) into molecular dioxygen. Note that in water suspensions, the lines of EPR signals are systematically broader for Cu^{2+}-substituted nanoparticles (Fig. 8c and d) than those for copper-free ones (Fig. 8a and b). This line broadening is characteristic of spin-spin interactions between the DMPO-adducts and molecular dioxygen. Because the cuprous ions formed through Eq. (9) can in turn react with H_2O_2 molecules to form HO$^{\bullet}$ radicals according to Eq. (6) (Fenton-like reaction), cupric ions in both $Mg_{0.9}Cu_{0.1}O$ and $Mg_{0.9}Cu_{0.1}(OH)_2$ can thereby convert a part of superoxide radicals into hydroxyl radicals. The UVA exposure of these experimental systems had no effect on the DMPO-adducts production whether in their nature or their amount (data not shown). Hydroxyl radical is the most reactive among all ROS because it can initiate a free radical chain reaction leading to extensive lipid and organic peroxide formation in aerobically living organisms (oxidative stress) [71]. Although it is of moderate magnitude, this extra production of the highly toxic hydroxyl radicals promoted by cupric ions is likely behind the significant enhancement of bactericidal performances of MgO and $Mg(OH)_2$ nanoparticles through the copper substitution. In Fig. 8, $Mg_{0.9}Cu_{0.1}(OH)_2$ nanoparticles produce more hydroxyl radical spin-adducts than $Mg_{0.9}Cu_{0.1}O$ ones (the same is true for $Mg(OH)_2$ and MgO nanoparticles). EPR study confirms that the high bactericidal activity reported for water suspension of $Mg_{1-x}Cu_xO$ nanoparticles is linked to that of $Mg_{1-x}Cu_x(OH)_2$ nanoparticles, progressively formed through the dissolution-precipitation process. It has been shown that carotenoid pigments as staphyloxanthin, giving the golden color to *S. aureus* bacteria envelope, have antioxidant properties [72] leading to H_2O_2 resistance [73]. These pigments can help these bacteria to detoxify hydroxyl radicals produced by copper-containing nanoparticles adsorbed onto their envelopes, thus decreasing their susceptibility to such antimicrobial treatment, especially for contact times as long as 180 min (Table S4). Deprived from this antioxidant molecule, no Gram-negative *E. coli* survive to 180 min of treatment with "hydroxylated" nanoparticles of copper-substituted MgO (Table S4).

4-Conclusion and perspective

Copper substitution together with nano-structuring were applied to increase the bactericidal performances of the rocksalt-type MgO oxide, known as periclase. The partial substitution of magnesium ions with Cu^{2+} has been successfully achieved in both micrometer- and nanometer-sized particles of MgO up to 20 mol%. In humid air at 20 °C, no surface hydroxylation of particles of a few microns in size occurred during the first 35 days of exposure whereas the sorption of water molecules by 10–20 nm-sized particles led to the growth a coherent hydroxide shell after 1 day only. Microstructural analyses using the Integral Breadth method reveal that the thermal decomposition of the single source precursor $Mg_{1-x}Cu_x(OH)_{2-2y}(CO_3)_y.zH_2O$ at 400 °C creates numerous defects in 10–20 nm-sized particles of $Mg_{1-x}Cu_xO$ thus obtained. These defects make the surface of nanoparticles highly reactive to the sorption of water molecules, to the extent that the cubic cell of as-prepared $Mg_{1-x}Cu_xO$ expands as soon as the nanoparticles are exposed to

ambient air (60% RH). The hydration in liquid water is based on the dissolution of $Mg_{1-x}Cu_xO$ particles and the released divalent cations precipitate as $Mg_{1-x}Cu_x(OH)_2$ as soon as the supersaturation is reached. Particles of a few microns in size dissolve all the more slowly the higher the copper content and only $Mg(OH)_2$ starts precipitating after 3 h. In contrast, the dissolution of all 10–20 nm-sized $Mg_{1-x}Cu_xO$ particles is complete over a 3 h period and water suspension only contains 4–12 nm-sized $Mg_{1-x}Cu_x(OH)_2$ particles at 3 h. Thereby, the bactericidal activity reported for water suspension of $Mg_{1-x}Cu_xO$ nanoparticles depends on the speed at which these nanoparticles dissolve and $Mg_{1-x}Cu_x(OH)_2$ precipitate in the first 3 h. Only 10 mol% of cupric ions in MgO nanoparticles are sufficient to kill both *E. coli* and *S. aureus* with bactericidal kinetics faster and reductions in viability at 3 h (6.5 Log_{10} and 2.7 Log_{10}, respectively) higher than the conventional CuO nanoparticles (4.7 Log_{10} and 2 Log_{10} in the same conditions). EPR spin trapping study reveals that "hydroxylated" $Mg_{0.9}Cu_{0.1}O$ as well $Mg_{0.9}Cu_{0.1}(OH)_2$ nanoparticles produce more spin-adducts with highly toxic hydroxyl radicals than their copper-free counterparts. The rapid mass adsorption of $Mg_{0.9}Cu_{0.1}(OH)_2$ nanoparticles onto the cell envelopes following their precipitation together with their ability to produce Reactive Oxygen Species are responsible for the exceptionally high bactericidal activity measured in the course of the hydroxylation of $Mg_{0.9}Cu_{0.1}O$ nanoparticles. In practical use, bactericidal materials are not always immersed in liquid water but solely exposed to ambient air with variable RH. As a hydroxide shell forms around the $Mg_{1-x}Cu_xO$ nanoparticles on contact with water vapor, the bactericidal activity measured will therefore depend strongly on RH. To overcome the problem, the use of copper-substituted $Mg(OH)_2$ hydroxide as bactericidal material shall be privileged to the oxide analogue.

Authorship contribution

Batiste CLAVIER: Investigation, Formal analysis, Visualization.

Téo BAPTISTE: Investigation.

Zuzana BARBIERIKOVÁ: Investigation, Visualization **(Electron Paramagnetic Resonance).**

Tomáš HAJDU: Investigation, Visualization **(Electron Paramagnetic Resonance).**

Amandine GUIET: Investigation (Transmission Electron Microscopy).

Fabien BOUCHER: Investigation (Atomic Emission Spectroscopy).

Vlasta BREZOVÁ: Methodology, **Investigation, Data Curation (Electron Paramagnetic Resonance).**

Christine ROQUES: Methodology, Investigation, **Data Curation (Bactericidal activity).**

Gwenaël CORBEL: Conceptualization, Methodology, Validation, Formal analysis, **Data Curation,** Writing- Original draft, Writing - Review & Editing, Visualization, Supervision, Project administration, Funding acquisition.

Declaration of competing interest

The authors declare that they have no known competing financial interests or personal relationships that could have appeared to influence the work reported in this paper.

Acknowledgement

The French Ministry of Higher Education, Research and Innovation and Le Mans University are acknowledged for providing a doctoral grant to BC. The EPR study was financially supported by Scientific Grant Agency of the Ministry of Education, Science, Research and Sport of the Slovak Republic (VEGA Project 1 /0026/18).

Appendix A - Supplementary data

Electronic Supplementary Data available: 1. Experimental details. 2. Crystallographic data. 3. Scanning Electron Microscopy (SEM) images of micrometer-sized $Mg_{1-x}Cu_xO$ particles. 4. Bactericidal activity reported for micrometer- and nanometer-sized $Mg_{1-x}Cu_xO$ particles. 5. EPR spectra of aerated water and DMSO/water suspensions of MgO, $Mg_{0.9}Cu_{0.1}O$ and $Mg_{0.9}Cu_{0.1}(OH)_2$ nanoparticles in the presence of DMPO spin trapping agent. Supplementary data to this article can be found online at doi:https://doi.org/10.1016/j.msec.2021.111997.

References

[1] Santé Publique France. Enquête nationale de prévalence des infections nosocomiales et des traitements anti-infectieux en établissements de santé, mai-juin 2017 (https://www.santepubliquefrance.fr/maladies-et-traumatismes/infections-associees-aux-soins-et-resistance-aux-antibiotiques/infections-associees-aux-soins/documents/enquetes-etudes/enquete-nationale-de-prevalence-des-infections-nosocomiales-et-des-traitements-anti-infectieux-en-etablissements-de-sante-mai-juin-2017), (2019) 1–270.

[2] L. Huang, D.-Q. Li, Y.-J. Lin, M. Wei, D.G. Evans, X. Duan, Controllable preparation of Nano-MgO and investigation of its bactericidal properties, J. Inorg. Biochem. 99 (2005) 986–993, https://doi.org/10.1016/j.jinorgbio.2004.12.022.

[3] S. Makhluf, R. Dror, Y. Nitzan, Y. Abramovich, R. Jelinek, A. Gedanken, Microwave-assisted synthesis of nanocrystalline MgO and its use as a bacteriocide, Adv. Funct. Mater. 15 (2005) 1708–1715, https://doi.org/10.1002/adfm.200500029.

[4] G. Applerot, J. Lellouche, A. Lipovsky, Y. Nitzan, R. Lubart, A. Gedanken, E. Banin, Understanding the antibacterial mechanism of CuO nanoparticles: revealing the route of induced oxidative stress, Small 8 (2012) 3326–3337, https://doi.org/10.1002/smll.201200772.

[5] A. Azam, A.S. Ahmed, M. Oves, M.S. Khan, A. Memic, Size-dependent antimicrobial properties of CuO nanoparticles against Gram-positive and -negative bacterial strains, Int. J. Nanomedicine 7 (2012) 3527–3535, https://doi.org/10.2147/ijn.s29020.

[6] A.F. Halbus, T.S. Horozov, V.N. Paunov, Strongly enhanced antibacterial action of copper oxide nanoparticles with boronic acid surface functionality, ACS Appl. Mater. Interfaces 11 (2019) 12232–12243, https://doi.org/10.1021/acsami.8b21862.

[7] V. Aruoja, S. Pokhrel, M. Sihtmae, M. Mortimer, L. Madler, A. Kahru, Toxicity of 12 metal-based nanoparticles to algae, bacteria and protozoa, Environmental Science: Nano 2 (2015) 630–644, https://doi.org/10.1039/C5EN00057B.

[8] G.L. Smithson, N.N. Bakhshi, The kinetics and mechanism of the hydration of magnesium oxide in a batch reactor, Can. J. Chem. Eng. 47 (1969) 508–513, https://doi.org/10.1002/cjce.5450470602.

[9] X. Pan, Y. Wang, Z. Chen, D. Pan, Y. Cheng, Z. Liu, Z. Lin, X. Guan, Investigation of antibacterial activity and related mechanism of a series of nano-$Mg(OH)_2$, ACS Appl. Mater. Interfaces 5 (2013) 1137–1142, https://doi.org/10.1021/am302910q.

[10] R.M. Hazen, Effects of temperature and pressure on the cell dimension and X-ray temperature factors of periclase, Am. Mineral. 61 (1976) 266–271.

[11] S. Asbrink, L.-J. Norrby, A refinement of the crystal structure of copper(II) oxide with a discussion of some exceptional e.s.d.'s, Acta Crystallographica Section B 26 (1970) 8–15, https://doi.org/10.1107/S0567740870001838.

[12] M. Paranthaman, K.A. David, T.B. Lindemer, Phase equilibria of the MgO-Cu_2O-CuO system, Mater. Res. Bull. 32 (1997) 165–173, https://doi.org/10.1016/S0025-5408(96)00184-5.

[13] T. Ohira, M. Kawamura, Y. Iida, M. Fukuda, O. Yamamoto, Influence of the mixing ratio on antibacterial characteristics of MgO-ZnO solid solution in two phase coexistence region, J. Ceram. Soc. Jpn. 116 (2008) 1234–1237, https://doi.org/10.2109/jcersj2.116.1234.

[14] B. Clavier, T. Baptiste, F. Massuyeau, A. Jouanneaux, A. Guiet, F. Boucher, V. Fernandez, C. Roques, G. Corbel, Enhanced bactericidal activity of brucite through partial copper substitution, J. Mater. Chem. B 8 (2020) 100–113, https://doi.org/10.1039/C9TB01927H.

[15] S. Stoll, A. Schweiger, EasySpin, a comprehensive software package for spectral simulation and analysis in EPR, J. Magn. Reson. 178 (2006) 42–55, https://doi.org/10.1016/j.jmr.2005.08.013.

[16] H.M. Rietveld, Line profiles of neutron powder-diffraction peaks for structure refinement, Acta Crystallogr. 22 (1967) 151–152, https://doi.org/10.1107/s0365110x67000234.

[17] J. Rodriguez Carvajal, Recent advances in magnetic structure determination by neutron powder diffraction, Physica B 192 (1993) 55–69, https://doi.org/10.1016/0921-4526(93)90108-I.

[18] L. Vegard, Die Konstitution der Mischkristalle und die Raumfüllung der Atome, Z, Physik 5 (1921) 17–26, https://doi.org/10.1007/BF01349680.

[19] R.D. Shannon, Revised effective ionic radii and systematic studies of interatomic distances in halides and chalcogenides, Acta Crystallogr. A32 (1976) 751–767, https://doi.org/10.1107/S0567739476001551.

[20] R.I. Razouk, R.S. Mikhail, The hydration of magnesium oxide from the vapor phase, J. Phys. Chem. 62 (1958) 920–925, https://doi.org/10.1021/j150566a006.

[21] R.M. Spriggs, L.A. Brissette, T. Vasilos, Grain growth in fully dense magnesia, J. Am. Ceram. Soc., 47 (1964) 417–418. doi:https://doi.org/10.1111/j.1151-2916.1964.tb13848.x.

[22] J.I. Langford, A rapid method for analysing the breadths of diffraction and spectral lines using the Voigt function, J. Appl. Crystallogr. 11 (1978) 10–14, https://doi.org/10.1107/S0021889878012601.

[23] T.H. de Keijser, J.I. Langford, E.J. Mittemeijer, A.B.P. Vogels, Use of the Voigt function in a single-line method for the analysis of X-ray diffraction line broadening, J. Appl. Crystallogr. 15 (1982) 308–314, https://doi.org/10.1107/S0021889882012035.

[24] J.I. Langford, D. Louër, E.J. Sonneveld, J.W. Visser, Applications of total pattern fitting to a study of crystallite size and strain in zinc oxide powder, Powder Diffract. 1 (1986) 211–221, https://doi.org/10.1017/S0885715600011738.

[25] J.I. Langford, The use of the Voigt function in determining microstructural properties from diffraction data by means of pattern decomposition, National Institute of Standards and Technology Special Publication 846. Editors Prince and Stalick., International Conference "Accuracy in Powder Diffraction II", May 26–29, 1992 at NIST, Gaithersburg, MD, USA, (vol. 1992) 110–126.

[26] R.S. Gordon, W.D. Kingery, Thermal decomposition of brucite: I, electron and optical microscope studies, J. Am. Ceram. Soc. 49 (1966) 654–660, https://doi.org/10.1111/j.1151-2916.1966.tb13194.x.

[27] M.G. Kim, U. Dahmen, A.W. Searcy, Structural transformations in the decomposition of $Mg(OH)_2$ and $MgCO_3$, J. Am. Ceram. Soc. 70 (1987) 146–154, https://doi.org/10.1111/j.1151-2916.1987.tb04949.x.

[28] M.J. McKelvy, R. Sharma, A.V.G. Chizmeshya, R.W. Carpenter, K. Streib, Magnesium hydroxide dehydroxylation: *in situ* nanoscale observations of lamellar nucleation and growth, Chem. Mat. 13 (2001) 921–926, https://doi.org/10.1021/cm000676t.

[29] J. Green, Calcination of precipitated $Mg(OH)_2$ to active MgO in the production of refractory and chemical grade MgO, J. Mater. Sci. 18 (1983) 637–651, https://doi.org/10.1007/BF00745561.

[30] K. Nakamoto, Applications in inorganic chemistry, in: Infrared and Raman Spectra of Inorganic and Coordination Compounds, John Wiley & Sons, Inc., 2008, pp. 149–354.

[31] R. Martens, F. Freund, The potential energy curve of the proton and the dissociation energy of the OH^- ion in $Mg(OH)_2$, Phys. Status Solidi A 37 (1976) 97–104, https://doi.org/10.1002/pssa.2210370112.

[32] O. Fruhwirth, G.W. Herzog, I. Hollerer, A. Rachetti, Dissolution and hydration kinetics of MgO, Surface Technology 24 (1985) 301–317, https://doi.org/10.1016/0376-4583(85)90080-9.

[33] L.F. Amaral, I.R. Oliveira, R. Salomão, E. Frollini, V.C. Pandolfelli, Temperature and common-ion effect on magnesium oxide MgO hydration, Ceram. Int. 36 (2010) 1047–1054, https://doi.org/10.1016/j.ceramint.2009.12.009.

[34] D.R. Lide, CRC Handbook of Chemistry and Physics 2008–2009: A Ready-reference Book of Chemical and Physical Data, CRC Press, Boca Raton, Florida, USA, 2008.

[35] P. Patnaik, Handbook of Inorganic Chemicals, in, McGraw-Hill, USA, 2003.

[36] Y. Cudennec, A. Lecerf, Y. Gerault, Synthesis of $Cu(OH)_2$ and CuO by soft chemistry, Eur. J. Solid State Inorg. Chem. 32 (1995) 1013–1022.

[37] Y. Cudennec, A. Riou, Y. Gérault, A. Lecerf, Hypothèse cristallochimique des mécanismes de formation de CuO(s) et de $Cu(OH)_2$(s) à partir de $Na_2Cu(OH)_4$(s), Comptes Rendus de l'Académie des Sciences - Series IIC - Chemistry 3 (2000) 661–666, https://doi.org/10.1016/S1387-1609(00)01170-1.

[38] Y. Fukuda, K. Tanabe, Infrared study of carbon dioxide adsorbed on magnesium and calcium oxides, Bull. Chem. Soc. Jpn. 46 (1973) 1616–1619, https://doi.org/10.1246/bcsj.46.1616.

[39] D.A. Torres-Rodríguez, H. Pfeiffer, Thermokinetic analysis of the MgO surface carbonation process in the presence of water vapor, Thermochim. Acta 516 (2011) 74–78, https://doi.org/10.1016/j.tca.2011.01.021.

[40] J. Highfield, J. Bu, J. Fagerlund, R. Zevenhoven, The promoter effect of steam in gas-solid CO_2 mineralization, in: 11th International Conference on Carbon Dioxide Utilization (ICCDU XI), Dijon, France, 2011.

[41] J.T. Newberg, D.E. Starr, S. Yamamoto, S. Kaya, T. Kendelewicz, E.R. Mysak, S. Porsgaard, M.B. Salmeron, G.E. Brown, A. Nilsson, H. Bluhm, Autocatalytic surface hydroxylation of MgO (100) terrace sites observed under ambient conditions, J. Phys. Chem. C 115 (2011) 12864–12872, https://doi.org/10.1021/jp200235v.

[42] R. Salomão, L.R.M. Bittencourt, V.C. Pandolfelli, A novel approach for magnesia hydration assessment in refractory castables, Ceram. Int. 33 (2007) 803–810, https://doi.org/10.1016/j.ceramint.2006.01.004.

[43] J. Bessières, A. Bessières, J.J. Heizmann, Iron oxide reduction kinetics by hydrogen, Int. J. Hydrog. Energy 5 (1980) 585–595, https://doi.org/10.1016/0360-3199(80)90037-3.

[44] J. Sloczyn'ski, W. Bobin'ski, Autocatalytic effect in the processes of metal oxide reduction. I. Kinetic model of the reduction, J. Solid State Chem., 92 (1991) 420–435. doi:https://doi.org/10.1016/0022-4596(91)90349-M.

[45] N.-Y.T. Nguyen, N. Grelling, C.L. Wetteland, R. Rosario, H. Liu, Antimicrobial activities and mechanisms of magnesium oxide nanoparticles (nMgO) against pathogenic bacteria, yeasts, and biofilms, Sci. Rep. 8 (2018), 16260, https://doi.org/10.1038/s41598-018-34567-5.

[46] C.L. Wetteland, N.-Y.T. Nguyen, H. Liu, Concentration-dependent behaviors of bone marrow derived mesenchymal stem cells and infectious bacteria toward magnesium oxide nanoparticles, Acta Biomater. 35 (2016) 341–356, https://doi.org/10.1016/j.actbio.2016.02.032.

[47] J. Sawai, E. Kawada, F. Kanou, H. Igarashi, A. Hashimoto, T. Kokugan, M. Shimizu, Detection of active oxygen generated from ceramic powders having antibacterial activity, Journal of Chemical Engineering of Japan 29 (1996) 627–633, https://doi.org/10.1252/jcej.29.627.

[48] C. Gunawan, W.Y. Teoh, C.P. Marquis, R. Amal, Cytotoxic origin of copper(II) oxide nanoparticles: comparative studies with micron-sized particles, leachate, and metal salts, ACS Nano 5 (2011) 7214–7225, https://doi.org/10.1021/nn2020248.

[49] O. Menkissoglu, S.E. Lindow, Relationship of free ionic copper and toxicity to bacteria in solutions of organic-compounds, Phytopathology 81 (1991) 1258–1263, https://doi.org/10.1094/Phyto-81-1258.

[50] C.L. Wetteland, J. de Jesus Sanchez, C.A. Silken, N.-Y.T. Nguyen, O. Mahmood, H. Liu, Dissociation of magnesium oxide and magnesium hydroxide nanoparticles in physiologically relevant fluids, J. Nanopart. Res. 20 (2018) 215, https://doi.org/10.1007/s11051-018-4314-3.

[51] M. Hans, A. Erbe, S. Mathews, Y. Chen, M. Solioz, F. Mücklich, Role of copper oxides in contact killing of bacteria, Langmuir 29 (2013) 16160–16166, https://doi.org/10.1021/la404091z.

[52] J. Sawai, H. Kojima, H. Igarashi, A. Hashimoto, S. Shoji, T. Sawaki, A. Hakoda, E. Kawada, T. Kokugan, M. Shimizu, Antibacterial characteristics of magnesium oxide powder, World J. Microbiol. Biotechnol. 16 (2000) 187–194, https://doi.org/10.1023/A:1008916209784.

[53] J. Sawai, T. Yoshikawa, Quantitative evaluation of antifungal activity of metallic oxide powders (MgO, CaO and ZnO) by an indirect conductimetric assay, J. Appl. Microbiol. 96 (2004) 803–809, https://doi.org/10.1111/j.1365-2672.2004.02234.x.

[54] A.F. Mendonca, T.L. Amoroso, S.J. Knabel, Destruction of gram-negative food-borne pathogens by high pH involves disruption of the cytoplasmic membrane, Appl. Environ. Microbiol. 60 (1994) 4009–4014, https://doi.org/10.1128/AEM.60.11.4009-4014.1994.

[55] Z.H. Zhao, Y. Sakagami, T. Osaka, Relationship between residual metal ions in a solution and the inhibitory capability of the metal ions for pathogenic bacterial growth, Bull. Chem. Soc. Jpn. 71 (1998) 939–945, https://doi.org/10.1246/bcsj.71.939.

[56] O. Akhavan, R. Azimirad, S. Safa, E. Hasani, $CuO/Cu(OH)_2$ hierarchical nanostructures as bactericidal photocatalysts, J. Mater. Chem. 21 (2011) 9634–9640, https://doi.org/10.1039/C0JM04364H.

[57] Z.M. Galbács, L.J. Csányi, Alkali-induced decomposition of hydrogen peroxide, J. Chem. Soc. Dalton Trans. 11 (1983) 2353–2357, https://doi.org/10.1039/DT9830002353.

[58] L.J. Csányi, L. Nagy, Z.M. Galbács, I. Horváth, Alkali-induced generation of superoxide and hydroxyl radicals from aqueous hydrogen peroxide solution, Z. Phys. Chem., 138 (1983) 107–116. doi:https://doi.org/10.1524/zpch.1983.138.1.107.

[59] D. Dong, G.F. Vandegrift, Alkaline peroxide processing of low-enriched uranium targets for ^{99}Mo production—decomposition of hydrogen peroxide, Nucl, Sci. Eng. 126 (1997) 213–223, https://doi.org/10.13182/NSE97-A24474.

[60] C.M. Miller, R.L. Valentine, Mechanistic studies of surface catalyzed H_2O_2 decomposition and contaminant degradation in the presence of sand, Water Res. 33 (1999) 2805–2816, https://doi.org/10.1016/S0043-1354(98)00500-4.

[61] A.N. Pham, G. Xing, C.J. Miller, T.D. Waite, Fenton-like copper redox chemistry revisited: hydrogen peroxide and superoxide mediation of copper-catalyzed oxidant production, J. Catal. 301 (2013) 54–64, https://doi.org/10.1016/j.jcat.2013.01.025.

[62] T.T.M. Nguyen, H.-J. Park, J.Y. Kim, H.-E. Kim, H. Lee, J. Yoon, C. Lee, Microbial inactivation by cupric ion in combination with H_2O_2: role of reactive oxidants, Environmental Science & Technology 47 (2013) 13661–13667, https://doi.org/10.1021/es403155a.

[63] W. Dröge, Free radicals in the physiological control of cell function, Physiol. Rev. 82 (2002) 47–95, https://doi.org/10.1152/physrev.00018.2001.

[64] C.D. Pericone, K. Overweg, P.W.M. Hermans, J.N. Weiser, Inhibitory and bactericidal effects of hydrogen peroxide production by *Streptococcus pneumoniae* on other inhabitants of the upper respiratory tract, Infect. Immun. 68 (2000) 3990, https://doi.org/10.1128/IAI.68.7.3990-3997.2000.

[65] M. Hricovíni, M. Mazúr, A. Sîrbu, O. Palamarciuc, V.B. Arion, V. Brezová, Copper (II) thiosemicarbazone complexes and their proligands upon UVA irradiation: an EPR and spectrophotometric steady-state study, Molecules 23 (2018) 17, https://doi.org/10.3390/molecules23040721.

[66] D. Dvoranová, Z. Barbieriková, M. Mazúr, E.I. García-López, G. Marcì, K. Lušpai, V. Brezová, EPR investigations of polymeric and H_2O_2-modified C_3N_4-based photocatalysts, J. Photochem. Photobiol. A Chem., 375 (2019) 100–113. doi: https://doi.org/10.1016/j.jphotochem.2019.02.006.

[67] A. Allouch, R.P. Lauricella, B.N. Tuccio, Effect of pH on superoxide/hydroperoxyl radical trapping by nitrones: an EPR/kinetic study, Mol. Phys. 105 (2007) 2017–2024, https://doi.org/10.1080/00268970701494024.

[68] E. Finkelstein, G.M. Rosen, E.J. Rauckman, Spin trapping. Kinetics of the reaction of superoxide and hydroxyl radicals with nitrones, J. Am. Chem. Soc. 102 (1980) 4994–4999, https://doi.org/10.1021/ja00535a029.

[69] M. Hayyan, M.A. Hashim, I.M. AlNashef, Superoxide ion: generation and chemical implications, Chem. Rev. 116 (2016) 3029–3085, https://doi.org/10.1021/acs.chemrev.5b00407.

[70] D. Dvoranová, Z. Barbieriková, V. Brezová, Radical intermediates in photoinduced reactions on TiO_2 (an EPR spin trapping study), Molecules 19 (2014) 17279–17304, https://doi.org/10.3390/molecules191117279.

[71] B. Chance, H. Sies, A. Boveris, Hydroperoxide metabolism in mammalian organs, Physiol. Rev. 59 (1979) 527–605, https://doi.org/10.1152/physrev.1979.59.3.527.
[72] G.Y. Liu, A. Essex, J.T. Buchanan, V. Datta, H.M. Hoffman, J.F. Bastian, J. Fierer, V. Nizet, *Staphylococcus aureus* golden pigment impairs neutrophil killing and promotes virulence through its antioxidant activity, J. Exp. Med. 202 (2005) 209–215, https://doi.org/10.1084/jem.20050846.
[73] V. Antonic, A. Stojadinovic, B. Zhang, M.J. Izadjoo, M. Alavi, *Pseudomonas aeruginosa* induces pigment production and enhances virulence in a white phenotypic variant of *Staphylococcus aureus*, Infect Drug Resist 6 (2013) 175–186, https://doi.org/10.2147/IDR.S49039.